

PL-TR-94-2199

AD-A286 638



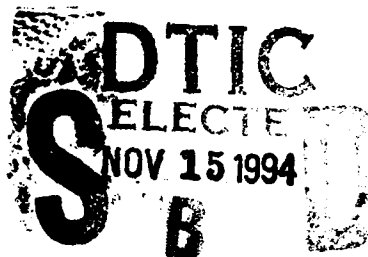
REAL-DATA TESTS OF A SINGLE-DOPPLER RADAR ASSIMILATION SYSTEM

Thomas Nehrkorn
James Hegarty
Thomas M. Hamill

Atmospheric and Environmental Research, Inc.
840 Memorial Drive
Cambridge, MA 02139

June 30, 1994

Scientific Report No. 5



Approved for public release; distribution unlimited



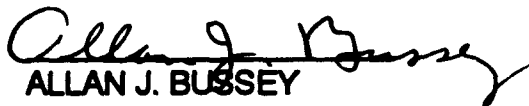
PHILLIPS LABORATORY
Directorate of Geophysics
AIR FORCE MATERIEL COMMAND
HANSCOM AIR FORCE BASE, MA 01731-3010

SS 94-35248

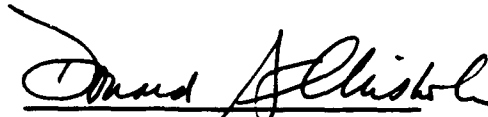
DTIC QUALITY INSPECTED 8

94 11 15 060

"This technical report has been reviewed and is approved for publication."



ALLAN J. BUSSEY
Contract Manager



DONALD A. CHISHOLM
Chief, Satellite Analysis and Weather
Prediction Branch
Atmospheric Sciences Division



ROBERT A. McCLATCHEY, Director
Atmospheric Sciences Division

This report has been reviewed by the ESC Public Affairs Office (PA) and is releasable to the National Technical Information Service (NTIS).

Qualified requestors may obtain additional copies from the Defense Technical Information Center (DTIC). All others should apply to the National Technical Information Service (NTIS).

If your address has changed, or if you wish to be removed from the mailing list, or if the addressee is no longer employed by your organization, please notify PL/TSI, 29 Randolph Road, Hanscom AFB, MA 01731-3010. This will assist us in maintaining a current mailing list.

Do not return copies of this report unless contractual obligations or notices on a specific document requires that it be returned.

REPORT DOCUMENTATION PAGE			Form Approved OMB No. 0704-0188	
Public reporting burden for this collection of information is estimated to average 1 hour per response, including the time for reviewing instructions, searching existing data sources, gathering and maintaining the data needed, and completing and reviewing the collection of information. Send comments regarding this burden estimate or any other aspect of this collection of information, including suggestions for reducing this burden, to Washington Headquarters Services, Directorate for Information Operations and Reports, 1215 Jefferson Davis Highway, Suite 1204, Arlington, VA 22202-4302, and to the Office of Management and Budget, Paperwork Reduction Project (0704-0188), Washington, DC 20503				
1. AGENCY USE ONLY (Leave blank)		2. REPORT DATE 30 June 1994		3. REPORT TYPE AND DATES COVERED Scientific No. 5
4. TITLE AND SUBTITLE Real-Data Tests of a Single-Doppler Radar Assimilation System			5. FUNDING NUMBERS F19628-91-C-0011 PE 62101F PR 6670 TA 17 WU CA	
6. AUTHOR(S) Thomas Nehrkorn, James Hegarty, Thomas M. Hamill				
7. PERFORMING ORGANIZATION NAME(S) AND ADDRESS(ES) Atmospheric and Environmental Research, Inc. 840 Memorial Drive Cambridge, MA 02139			8. PERFORMING ORGANIZATION REPORT NUMBER (none)	
9. SPONSORING/MONITORING AGENCY NAME(S) AND ADDRESS(ES) Phillips Laboratory 29 Randolph Road Hanscom AFB, MA 01731-3010 Contract Monitor: Allan Bussey/GPAB			10. SPONSORING/MONITORING AGENCY REPORT NUMBER PL-TR-94-2199	
11. SUPPLEMENTARY NOTES				
12a. DISTRIBUTION/AVAILABILITY STATEMENT Approved for public release; distribution unlimited			12b. DISTRIBUTION CODE	
13. ABSTRACT (Maximum 200 words) Real data tests of a single-Doppler radar data assimilation and forecast system have been conducted for a Florida sea breeze case. The system consists of a hydrostatic mesoscale model used for prediction of the preconvective boundary layer, an objective analysis that combines model first guess fields with radar derived horizontal winds, a thermodynamic retrieval scheme that obtains temperature information from the three-dimensional wind field and its temporal evolution, and a Newtonian nudging scheme for forcing the model forecast to closer agreement with the analysis. As was found in earlier experiments with simulated data, assimilation using Newtonian nudging benefits from temperature data in addition to wind data. The thermodynamic retrieval technique was successful in retrieving a horizontal temperature gradient from the radar-derived wind fields that, when assimilated into the model, led to a significantly improved forecast of the seabreeze strength and position.				
14. SUBJECT TERMS Convection Seabreeze Single Doppler Radar Thermodynamic Retrieval			15. NUMBER OF PAGES 56	
			16. PRICE CODE	
17. SECURITY CLASSIFICATION OF REPORT Unclassified	18. SECURITY CLASSIFICATION OF THIS PAGE Unclassified	19. SECURITY CLASSIFICATION OF ABSTRACT Unclassified	20. LIMITATION OF ABSTRACT SAR	

Table of Contents

Page

1. Introduction	1
2. The Prototype Assimilation and Forecast System	2
2.1. The mesoscale forecast model	2
2.2. Radial wind extraction (SPRINT)	3
2.3. Radial and tangential wind extraction (TREC)	3
2.4. Objective analysis of winds	4
2.5. Thermodynamic retrieval	5
2.6. Newtonian nudging	7
3. Case Selection	7
3.1. General remarks	7
3.2. The 23 July case	9
4. Assimilation Experiments	11
4.1. General remarks	11
4.2. Control run	11
4.3. Wind-only assimilation	13
4.4. Wind and temperature assimilation	15
5. Summary and Conclusions	17
6. References	18

Accession For	
HTIS GRA&I	<input checked="checked" type="checkbox"/>
DTIC TAB	<input type="checkbox"/>
Unannounced	<input type="checkbox"/>
Justification	
By	
Distribution	
Availability Codes	
Dist	Avail and/or Special
A-1	

List of Figures

Page

1	Plots of PAM surface data. Station locations correspond to the origin of the wind vectors; potential temperature is plotted above and to the left of the station location.....	20
2	TREC derived winds valid for 1705 UTC, over the same geographic region and with the same wind vector scale as in Figure 1, for elevation angles 0.3°, 0.9°, 1.5°, and 2.1°.	24
3	Fractional area of PL-3D gridpoints covered by water. Model domain shown corresponds to the area plotted in Figure 1.....	26
4	The sounding used to initialize the model runs: potential temperature - top panel, u (solid) and v (dotted) - bottom panel.....	27
5	Horizontal cross section of winds and θ at level 2, and vertical cross section at $y=0$, for hour 2 (16 UTC) of the control run.	28
6	Horizontal cross section of winds and θ at level 2, and vertical cross section at $y=0$, for hour 4 (18 UTC) of the control run.	29
7	Horizontal cross section of winds and θ at level 2, and vertical cross section at $y=0$, for hour 6 (20 UTC) of the control run.	30
8	Horizontal cross sections of winds and θ at level 4 for hours 2, 4, and 6 (16, 18, and 20 UTC) of the control run.....	31
9	Vertical cross section of winds and θ at $y=+25$ km, for hours 2, 4, and 6 of the control run.	33
10	Horizontal cross section of winds and θ at level 2 for hour 3 (17 UTC) of the wind-only assimilation: first guess, analysis, and analysis increments.....	35
11	Horizontal cross section of winds and θ for level 2 at hour 4 (18 UTC): wind-only assimilation and differences from control	37
12	Vertical cross section of winds and θ at $y=0$ for hour 4 (18 UTC): wind-only assimilation and differences from control	38
13	Horizontal cross section of winds and θ at level 2 for hour 6 (20 UTC): wind-only assimilation and differences from control	39

List of Figures (continued)**Page**

14	Vertical cross section of winds and θ at $y=0$ for hour 6 (20 UTC): wind-only assimilation and differences from control	40
15	Horizontal cross section of winds and θ at level 2 for hour 3 (17 UTC) of the full assimilation: first guess, analysis, and analysis increments.....	41
16	Horizontal cross section of winds and θ at level 4 for hour 3 (17 UTC) of the full assimilation: first guess, analysis, and analysis increments.....	42
17	Horizontal cross section of winds and θ at level 2 for hour 4 (18 UTC): full assimilation and differences from control	43
18	Horizontal cross section of winds and θ at level 4 for hour 4 (18 UTC): full assimilation and differences from control	44
19	Vertical cross section of winds and θ at $y=0$ for hour 4 (18 UTC): full assimilation and differences from control	45
20	Horizontal cross section of winds and θ at level 2 for hour 6 (20 UTC): full assimilation and differences from control	46
21	Horizontal cross section of winds and θ at level 4 for hour 6 (20 UTC): full assimilation and differences from control	47
22	Vertical cross section of winds and θ at $y=0$ for hour 6 (20 UTC): full assimilation and differences from control.....	48
23	Horizontal cross section at level 2, and vertical cross section at $y=0$, of winds and θ for hour 6 (20 UTC): differences between full assimilation and wind-only assimilation	49

1. Introduction

This technical report is the last report in a series of three reports describing our research into the feasibility of thunderstorm prediction based on the continuous assimilation of single-Doppler radar information into a numerical forecast model. This research is motivated by several factors: the introduction of the WSR-88D (formerly called NEXRAD) network of single Doppler radars makes this data source widely available; the onset of convection has been linked to low-level convergence (Wilson and Schreiber, 1986); and clear-air returns from 3-5 cm radars in the preconvective boundary layer (from seeds and insects) are sufficient to allow determination of radial velocities (Kropfli, 1986). The approach taken in our research was to use a simple, hydrostatic mesoscale model to predict the evolution of the boundary layer, and to assimilate single-Doppler radar observations into the model to improve the forecast. Nowcasts and forecasts from the mesoscale model could then be used to identify present and future regions of boundary layer convergence, which would be areas of preferential thunderstorm initiation. We concentrated on the Florida sea breeze in our work, because of the well-established success of mesoscale models in simulating the sea breeze, and the availability of data from the Convection and Precipitation/Electrification (CaPE) experiment conducted over Florida in 1991.

The first report in the series (Hamill, 1992) describes the forecast model used in this study (PL3D - a hydrostatic version of the Colorado State University Regional Atmospheric Modeling System (CSU RAMS)) and the results of observing system simulation experiments demonstrating the importance of assimilating wind and temperature data, rather than just wind data. This confirmed the results by Liou (1989) and Cotton et al. (1989) that assimilation using Newtonian nudging (Stauffer and Seaman, 1990) of the observed Doppler wind velocities alone is usually insufficient; temperature information is also needed. Without temperature information, circulation patterns developed from the assimilation of wind data may not be sustained. In the preconvective boundary layer, areas with low-level convergence are usually also areas with positive buoyancy. As was shown in Cotton et al. (1989), nudging the winds alone in this situation may actually create a cold anomaly through adiabatic cooling, resulting in the circulation reversing direction after the nudging is stopped. Our own assimilation experiments using wind data alone (Hamill,

1992) for a seabreeze simulation also showed generally inferior forecasts compared to those experiments with nudging to observed winds and temperatures.

The approach taken in our research is to "retrieve" atmospheric temperatures from the measured wind field. Provided the winds are known with reasonable accuracy, the temperature field can be deduced from the three-dimensional distribution of the wind field and its temporal evolution, because the two are linked through the equations of motion (Gal-Chen, 1986). Because single Doppler radar measurements only provide the radial component of the wind, we have designed a multi-step prototype forecast and assimilation system. The first step is to extract as much information as possible about the 3-D windflow from a single-Doppler radar using two algorithms, one of which produces observations with not only radial but also tangential wind velocities. Both types of Doppler-derived observations are then combined with a model forecast through a simple objective analysis and the resultant wind analyses drive the Gal-Chen temperature retrieval. With high-resolution analyzed fields of wind and temperature, the simple mesoscale model forecast is then nudged toward a more realistic description of the atmosphere, presumably resulting in a more realistic forecast.

The second technical report (Hamill and Nehrkorn, 1993) describes our implementation of this technique, and results from tests with simulated data. In this report we describe tests of our prototype system with real data. We briefly review the assimilation procedure in Section 2, but for a more detailed description the reader is referred to Hamill and Nehrkorn (1993). The case selection from the CaPE experiment data is described in Section 3, the results of the assimilation experiments are described in Section 4, and Section 5 contains a summary and conclusions.

2. The Prototype Assimilation and Forecast System

2.1. The mesoscale forecast model

The PL-3D mesoscale model is a modified, hydrostatic version of the CSU RAMS (Tripoli and Cotton, 1982). It is described fully in Gustafson et al. (1991) and Cotton et al. (1989), and references contained therein. Its governing equations are the hydrostatic equations of motion, with prognostic variables u , v , and θ (horizontal wind and potential temperature). Thermodynamic variables

are decomposed into a horizontally uniform, time-invariant basic state, and deviations from this state. The pressure field (in the form of the Exner function¹) is diagnosed from the hydrostatic equation, and the vertical velocity from the anelastic continuity equation where only variations of the basic-state density are considered. It includes a first-order turbulence closure where diffusion coefficients are a function of the vertical deformation and the Richardson number, a soil heat transfer parameterization, and a radiation package that allows a simulation of the planetary boundary layer. Water vapor is treated as a passive tracer only in this version and moist processes (condensation and precipitation physics) are ignored. It uses a staggered grid in the horizontal and vertical and allows for a terrain-following vertical coordinate, though a flat terrain is used in these simulations. The equations are solved with a time-split scheme, which uses a smaller time step for terms which admit the fast Lamb wave. Advective terms are computed using a second-order accurate forward-in-time upstream advective operator.

2.2. Radial wind extraction (SPRINT)

The SPRINT (Sorted Position Radar INterpolation) software, developed at the National Center for Atmospheric Research, performs a Cartesian rectification of Doppler measurements (Mohr et al., 1986). It is used to grid the Doppler radial velocities at regular time intervals, making them available to the objective analysis software. SPRINT software is typically used in the gridding of dual-Doppler data; however, for our purposes it was used to grid single-Doppler radial wind components. The SPRINT software was obtained from NCAR and installed on the Cray-YMP of the Army Waterways Experiment Site (WES). The output format was modified to facilitate the transfer of the data to the AIMS system and its ingest by the objective analysis software.

2.3. Radial and tangential wind extraction (TREC)

TREC is the "Tracking of Radar Echoes by Correlation" (Tuttle and Foote, 1990). This technique can be used to infer a 2-D wind field from successive scans of measured reflectivities. It does this through a cross-correlation of subsets of a

¹For a definition of the Exner function, see Pielke (1984).

scan of radar data at time T to all surrounding subsets for a scan at time $T + \Delta T$. The displacement vector (i.e., "wind") is from the center of the originating box to the center of the box with the maximum correlation. This scheme is very useful because it is currently the only scheme which can derive relatively high-resolution boundary layer wind inferences with both radial and *tangential* components. However, the TREC scheme is sensitive to ground clutter, works best with closely timed radar scans (3-5 minutes between successive scans is ideal) and requires clear-air inhomogeneities or scatterers such as bugs to use as passive tracers. TREC provides information on the movement of features. Features do not necessarily move with the wind. Insect migration and wave propagation can contribute to the movement of radar features in a direction that differs from the wind. TREC does not provide "wind observations" but, rather, information on features movement. For clear air situations, the movement of features is perhaps better correlated with wind direction than for precipitation situations, but it is important to note that the wind interpretation can be in serious error. The TREC software was obtained from the author (John Tuttle, at NCAR) and installed on the WES Cray-YMP. The code was modified to change output format and the graphical output routines were moved to a stand-alone program to be run on the AER computer system.

2.4. Objective analysis of winds

This step adjusts a model first guess of the wind field to wind velocity observations from TREC and gridded radial velocities from SPRINT. This objective analysis is based on the technique of successive corrections (Cressman, 1959), but differs in some substantive ways from the basic Cressman scheme. The major differences are as follows:

a. Analysis in radial/tangential coordinate system. It is traditional to perform the objective analysis on the u- and v-components of the wind. With the current code, the analysis is done on radial and tangential components and converted back to u/v as a last step. This is done because the TREC scheme supplies observations with both a radial and tangential component, but the SPRINT output has only radial velocities. Analyzing in the conventional u/v coordinate system would require a prior step of inferring some tangential component of the wind for the SPRINT observations - a step liable to induce error.

b. Use of only one SPRINT observation. For the SPRINT observations, only the derived radial velocity at a particular gridpoint is allowed to affect the analysis at that gridpoint; neighboring gridpoints' radial velocities are not used. Once again, this is due to the incomplete wind information having only radial velocities. Nearby gridpoints, especially close to the radar, will have a radial direction different from the radial direction at the analysis point; thus, it will not have complete information on the radial velocity at the original analysis point.

c. Use of nonstandard summation relation. The standard Cressman summation relation is replaced by one in which the weight given to an observation is not only a function of horizontal distance between the gridpoint and the observation, but also a function of the vertical separation between the observation and the gridpoint. In addition, weights are computed separately for TREC and SPRINT observations and normalized such that each type of observation contributes roughly equally to the analysis. The latter modification is introduced since only one SPRINT observation is available at a given gridpoint, whereas this gridpoint can be influenced by dozens of TREC observations. Uncorrected, this could have a deleterious influence on the quality of the objective analysis.

d. Use of a vertical weighting coefficient. We have developed a vertical weighting coefficient which allows the observation increments to be applied not only to the level of the observation but to surrounding vertical levels. This weight is of the form:

$$W_v = 1.0 / [1.0 + C_v * (D_h)^2] \quad (1)$$

where

W_v = derived vertical weight;

C_v = weighting coefficient (m^{-2}); and

D_h = height difference between observation and analysis level (m).

2.5. Thermodynamic retrieval

Following the method of Gal-Chen (1986) and the derivation of Liou (1989), temperature observations can be derived from gridded wind data. The basic approach is to rewrite the u- and v-equations such that the x-derivative (y-derivative) of pressure is on the left hand side and all other terms of the u-equation (v-equation) are on the right hand side: local time rate of change, horizontal and

vertical advection, Coriolis acceleration, and turbulent friction. With the available Doppler information, we can estimate all the terms on the right hand side: the horizontal winds are estimated from an objective analysis of Doppler radar data, the vertical velocities through the procedure described below, and the local time derivatives through comparisons of successive scans of Doppler wind analyses. In general, there will be no solution of the pressure field that satisfies both equations exactly, due to errors in the observational data, approximations of the governing equations, and their numerical solution. A least squares solution can be obtained as the solution of a Poisson equation. The solution, at any vertical level, is then known only to within an arbitrary additive constant. To remove this non-uniqueness, we impose the constraint that the horizontal mean of the derived pressure is equal to that of the model first guess. With the pressure determined, temperature can be retrieved, as will be shown later.

Specific algorithmic steps in the dynamic retrieval are:

- a. Calculation of vertical velocity. The PL-3D model normally calculates the vertical velocity from an upward integration of the continuity equation. For consistency, this was preserved here. However, because Doppler-derived wind analyses may be noisy, we chose to impose constraints on the diagnosed vertical velocities. The Doppler-derived vertical velocity was used nearly unchanged near the ground, but as the model layer height approached a prespecified height level ($Z(k_{\max})$), it was effectively damped toward that of the first guess.
- b. Calculation of u and v forcing functions. The forcing functions (right hand sides) of the u and v equations must be calculated using the available Doppler radar data. There are four general terms: the local rate of change, advection, coriolis, and turbulence. Existing CSU/RAMS code is used to calculate all terms except the local rate of change, which is calculated using a backward difference with the previous analysis.
- c. Dynamic Retrieval of Pressure Perturbations. Using standard numerical techniques such as sequential over-relaxation (Vemuri and Karplus, 1981) the Poisson equation for pressure is solved level by level. Layer mean temperatures are then computed from the analyzed pressure at surrounding analysis levels.

d. Extraction of Temperature Observations. The hydrostatic equation is written in finite difference form and solved for the mean layer temperatures. Level temperatures are then derived from the layer mean temperatures of the surrounding layers. A final check is made to ensure that no biases were introduced in the vertical interpolation. If necessary, temperatures are reset such that their horizontal average is equal to that of the first guess.

2.6. Newtonian nudging

Following the discussion in Hamill (1992) the model is now nudged to the new data adjusting the model's time tendencies for u , v , and θ according to:

$$F_{\text{tot}} = F_{\text{mod}} + (X_{\text{obs}} - X_{\text{mod}}) * R * W_t \quad (2)$$

where

F_{tot} = $\partial X / \partial t$ = total local tendency for the gridpoint at a given timestep;

F_{mod} = normal model terms of the local tendency (e.g., advection, coriolis);

X_{obs} = observed field's value for a gridpoint at time (t);

X_{mod} = model forecast value for a gridpoint at time (t);

R = nudging coefficient; and

W_t = weight applied to this timestep.

The residuals ($X_{\text{obs}} - X_{\text{mod}}$) are calculated at the time when the Doppler analysis and temperature retrieval are performed and the residual is used until the next analysis time. The nudging coefficient (R) used in these experiments was set at $5.56 \times 10^{-4} \text{ s}^{-1}$, corresponding to an adjustment time scale of 1800 sec. To deweight the residual as we progress forward in time, W_t starts at 1.0 at the time of the analysis but decreases, approaching zero right at the time of the next Doppler analysis and retrieval.

3. Case Selection

3.1. General remarks

The data source for our real data experiments was the CaPE experiment, which was conducted between 8 July and 18 August 1991 over Florida. The National Center for Atmospheric Research (NCAR) deployed three radars over the Cape Kennedy area. The dual wavelength (3 and 10 cm) CP2 radar was located at the coast line to the north of Cape Kennedy and used primarily for

quantitative measurements of rain, precipitation physics, and cloud electrification. A secondary role of the CPL radar was to support aircraft penetration and dual Doppler studies of convective cells. Of more interest for our purpose were the NCAR CP3 and CP4 radars, which are 5 cm Doppler radars capable of detecting air motions in the cloud-free boundary layer. They were located to the south of Cape Kennedy, CP4 close to the coast, and CP3 further inland. Locations of the CP2, CP3, and CP4 radars are indicated in Figure 1 by asterisks. The area shown in Figure 1 is a 160 km by 160 km area centered on the CP4 radar location, on a Mercator projection. Latitude/longitude scales are shown on the left/top margins. Also shown are the locations of the NCAR Portable Automated Mesonet (PAM) surface stations.

To test our prototype assimilation and forecast system, we looked for days which were initially quiescent, and then quickly developed large thunderstorms over the CaPE network, preferably in response to sea breeze forcing. Descriptions of the synoptic situation and the data collection efforts for the experiment days, contained in the CaPE experiment log (Williams et al., 1992), were reviewed for this purpose. In addition, we obtained video loops of visible GOES satellite imagery over the Florida area. While reviewing the loops of visible satellite imagery, it quickly became apparent that the scenario described above was less the rule than the exception. More likely, intense thunderstorm development was preceded by a more complex series of events. In many cases, small convective clouds did form along the sea-breeze front, but quickly dissipated. More significant thunderstorm development then typically followed from the interaction of the outflow boundaries from the initial cells. In one case, 27 July, outflow from convection that had formed along the Gulf Coast seabreeze and moved inland forced new, intense convective development when it collided with the Atlantic sea breeze front. Simulation and prediction of this series of events is clearly beyond the capabilities of the simple mesoscale model used in our study and the computational power expected to be available at typical forecast sites. We did, however, identify one case that fit the selection criteria. On 16 July, intense convection formed along the sea-breeze front, close to the Cape Kennedy area, making it a potential case for study.

For a closer examination of the radar data, we obtained a software package from NCAR's Atmospheric Technology Division's Research Branch to peruse and edit radar data. Examination of the CP2 radar data revealed that for the 16 July case, during the time for which survey scan data were available, the sea breeze front was still off-shore and thus not visible due to a lack of scatterers. The CP3 and CP4 data for that day had other problems: there was only one scan performed at a low enough elevation angle for usable boundary layer returns, thus making this dataset unusable for the thermodynamic retrieval technique.

Because of the severe constraints on vertical resolution of the radar data in the boundary layer imposed by the thermodynamic retrieval technique, we subsequently concentrated on experiment days during which the sea breeze was sampled well by the CP3 and CP4 radars, even if there was no significant development on that day along the sea breeze. This led to the final selection of 23 July as our real data test case. The meteorological situation and data coverage for this day are described in detail in the next section.

3.2. The 23 July case

The synoptic situation, as summarized in Williams et al. (1992), was characterized by a broad area of high pressure over Florida, with light and variable winds over the CaPE area. A land breeze existed during the night and early morning. Thunderstorms were primarily confined to an area well north of the CaPE area and there was no development in the area covered by the CP3 and CP4 radars, aside from a cell approximately 40 km to the SSW of CP4, which developed into a storm by 1946 UTC (1546 EDT).

The development of the seabreeze near Cape Kennedy can be seen from the sequence of plots of PAM data in Figure 1. At 14 UTC winds are generally light and variable, although the predominance of the off-shore direction suggests the presence of a land breeze. Potential temperatures are essentially uniform across the region aside from an obviously bad data point just south of CP3. One hour later, temperatures have risen by 1 - 2 K, except right near the coast, where increases are .5 K or less. On-shore winds are evident right along the coast line. This trend continues over the next hour, where, by 16 UTC the east-west gradient of potential temperature is between 1 - 1.5 K and on-shore winds of up to 4 m/s are evident along the coast. Along the line indicated in Figure 1.c, which extends

from 10 km east to 60 km west of CP4, the temperature difference is approximately 1.3 K. Over the course of the next two hours, the seabreeze convergence line strengthens and begins to move inland. At 17 UTC the on-shore winds along the coast have further strengthened and at 18 UTC winds are generally easterly 5-10 km inland. At that time, the temperature difference along the indicated line is approximately 2.4 K. At 19 UTC the seabreeze convergence line is just to the west of the CP3 radar, roughly 20 km west of the CP4 location. On-shore winds are still strongest along the coast, where wind speeds are in the 5 - 7.5 m/s range. Finally, at 20 UTC, easterly winds of up to 3 m/s can be found as far inland as 20 km and the temperature difference along the indicated line is increased to 2.7 K at that time.

The CP3 and CP4 radars both performed survey scans at several low elevation angles (0.5° , 0.9° , 1.5° , 2.1° , 2.7° , 3.3°) between 14:21 UTC and 18:04 UTC. Examination of the data from these radars revealed that the CP3 data would not be very useful for our purposes; since the view to the east was partially obstructed by trees and the seabreeze front did not penetrate very far inland before 18 UTC, there was no seabreeze signature evident in the returns received by CP3. However, the CP4 radar, while it did not provide any information about the flow over the water, did sample a significant portion of the developing seabreeze circulation both in the radial velocity fields and the derived TREC wind vectors. Figure 2 shows the wind vectors derived by the TREC technique from two successive scans centered at 1705 UTC (1659 - 1704 UTC, and 1706 - 1711 UTC), for the first four elevation angles. The data are shown on a radar-centered coordinate system with the x- and y-axis representing the eastward and northward distance from the CP4 radar. The geographic region and the wind vector scale are the same as in Figure 1. As the elevation angle is increased, boundary layer returns are restricted to smaller distances from the radar: at 2.1° , the highest angle used for the TREC technique, returns are only available out to less than 20 km. The TREC motions at that time are generally weak (less than 2-3 m/s) and somewhat disorganized, displaying a fair amount of small-scale variability.

4. Assimilation Experiments

4.1. General remarks

The model integrations described below were performed on a horizontal and vertical grid designed to facilitate ingest of CP4 radar data. The horizontal grid was centered at the CP4 radar location and a uniform horizontal grid spacing of 5 km was used to match the output of the SPRINT program. The coast-line used in the model is shown in Figure 3, which shows the fractional land area of each grid point. Vertical grid spacing was variable, varying between 200 m near the surface to 350 m at the top of the domain. Table 1 shows the location of the staggered levels (used for vertical velocity) and tracer levels (used for all other variables). A long time step of 10 sec and a small timestep of 5 sec was used. (The model uses a time-split integration scheme, using a small timestep for terms related to fast gravity wave motion.)

4.2. Control run

The forecast model was initialized at 14 UTC (10 EDT), using the 1404 UTC sounding (see Figure 4) taken at TYCO airport, which is located approximately halfway between the CP3 and CP2 radar sites. The sea surface temperature was set at 301 K, based on climatological values. Figure 5, which is a horizontal cross section at level 2 (the first model level above ground) at hour 2 of the forecast (16 UTC), shows a seabreeze circulation along the coast, with a temperature difference in excess of 2 K across the coastline. The vertical cross section through the CP4 radar location shown in the same figure shows the leading edge of the seabreeze and the associated updraft centered at $x = -10$ km, i.e. 10 km west of CP4, or roughly 16 km inland from the coastline. The temperature difference between $x = +10$ km and $x = -60$ km (at $y = 0$) is approximately 1.2 K. The updraft has moved 20 km further inland by hour 4 of the forecast (18 UTC; see Figure 6), and temperatures over land have risen by 2 K in response to solar heating, resulting in a 3-4 K east-west temperature difference². This trend continues to hour 6 of the forecast (Figure 7), at which time the circulation has further strengthened, temperatures inland have risen by another degree, and easterly

²Note that velocity vectors are plotted to reflect the exaggerated vertical scale of the Figures.

Table 1: Height of model levels in meters above ground.

Level	Stagger level (w)	Tracer Level (u,v, θ)
1	0	-100
2	200	100
3	400	300
4	600	500
5	800	700
6	1000	900
7	1200	1100
8	1400	1300
9	1600	1500
10	1800	1700
11	2000	1400
12	2200	2100
13	2400	2300
14	2600	2497
15	2850	2719
16	3150	2994
17	3500	3322
18	3850	3675
19	4200	4025
20	4550	4375
21	4900	4725
22	5250	5075

winds are evident throughout the domain with the seabreeze front updraft located at $x=-60$ km (at $y=0$ km). Figure 8 shows horizontal cross sections at level 4 (600 m) at hours 2, 4, and 6 of the forecast. The evolution is quite similar to that shown at level 2, but the temperature gradient is noticeably weaker. Vertical cross sections to the south of the radar (not shown) are very similar to the ones shown in Figures 6-8, except that the circulation is somewhat further to the east, in accordance with the shape of the coastline. Vertical cross sections to the north of CP4 (shown in Figure 9) show a somewhat disorganized secondary updraft pattern near $x=0$ at hour 2 of the forecast, which is a result of the complicated

coastline at that location. This feature is soon overwhelmed by the primary circulation, however. In earlier model integrations using a larger time step, a weak $2\Delta x$ vertical velocity pattern developed at this location, leading to strong numerical noise and an eventually unusable forecast.

Comparisons of the model output with the PAM data plots indicate that the seabreeze circulation is overpredicted by the model at the later stages of the forecast for this case. To facilitate comparison with PAM data, and the later assimilation experiments, key features of the seabreeze simulation are summarized in Table 2. For the PAM data, the location of the updraft maximum was estimated from the convergence of the low-level wind field. It is evident from the figures and Table 2 that at hour 2 (1600 UTC), the model simulation is still in general agreement with the observations, both in terms of the temperature gradient and the updraft location. At hour 4, the seabreeze front is approximately 10-20 km too far inland and land temperatures are too high by 1-2 K. By hour 6, the seabreeze front is almost 40 km too far inland and the temperature contrast between the coast and inland is almost 2 K too large.

There are a number of possible reasons for these forecast errors. The available atmospheric data indicate that there was no cloud cover or cold advection observed that day to account for the slower than predicted warming. Thus, the most likely reasons are related to parameter choices for the surface characteristics: the specified water temperature might be slightly too cool, leading to an exaggerated land-sea temperature contrast; the soil type and/or initial soil moisture might result in a soil that is too dry, leading to excessive warming of the ground; or the albedo might be too small, leading to excessive amounts of absorbed shortwave radiation. Since temperature errors are larger over land than water, the land surface characteristics are probably the most important factor. We did not attempt to tune the model any further for this forecast. Instead, we used assimilation of TREC and SPRINT winds and the derived temperature fields, to try to improve the forecast.

4.3. Wind-only assimilation

This model run is identical to the control run, except that the model is nudged toward the observed (TREC and SPRINT) winds between hours 2 and 4 of the forecast (between 16 UTC and 18 UTC). For this assimilation run, the

Table 2: Comparison of key features of the sea breeze between the PAM observations, the Control run, the Wind-only, and Full (wind and temperature) assimilation runs. Locations refer to the x-coordinate at $y=0$, and $\Delta T / 70$ km is the near-surface potential temperature difference between $x=+10$ km and $x=-60$ km at $y=0$.

Feature	Time	PAM obs	Control	Wind-only	Full
Updraft location		0 to -5 km	-5 km	-5 km	-5 km
Center of circulation	2 h 16 UTC		0 km	0 km	0 km
$\Delta T / 70$ km		1.2 K	1.2 K	1.2 K	1.2 K
Updraft location		-10 km	-25 km	-20 km	-10 km
Center of circulation	4 h 18 UTC		-15 km	-10 km	0 km
$\Delta T / 70$ km		2.4 K	3 K	2.9 K	2.4 K
Updraft location		-10 to -20 km	-50 km	-40 km	-35 km
Center of circulation	6 h 20 UTC		-40 km	-30 km	-20 km
$\Delta T / 70$ km		2.7 K	4.4 K	4.4 K	3.7 K

temperature retrieval step is skipped in the assimilation procedure. Radar data used for the assimilation consisted of full PPI scans at elevation angles 0.3° , 0.9° , 1.5° , and 2.1° between 1604 UTC and 1804 UTC, which were available every 7 minutes (aside from one 20 minute gap and three gaps of 10-13 minutes). Thus, both SPRINT and TREC winds were available throughout the assimilation period.

The objective analysis step of the radar-observed winds at the first model level is shown in Figure 10, which shows the wind and potential temperature fields before and after the objective analysis and the difference between the two (the analysis increments). Wherever radar observations are present, they result in a weakening of the easterly winds of the first guess, as is to be expected in light of the forecast errors evident from the PAM data. The largest increments are directly to the west of the CP4 radar, since the u-component of the wind is

sampled by both the SPRINT (radial) and TREC (total) winds. To the north and south of the radar, the radial components of the predicted and observed flow are small, so here the westerly analysis increments are a direct consequence of the use of TREC winds. Radar returns are absent over water, limiting the influence of the observations to near the coast line. Since no temperature retrieval is performed, there are no analysis increments of temperature. Analysis increments at level 4 (600 m, not shown) exhibit a generally similar pattern.

The effect of the assimilation on the forecast can be seen in Figure 11, which shows the fields at the end of the assimilation period and the differences from the control run. As is to be expected from the preceding discussion of the analysis increments, the effect of the wind assimilation is the weakening of the easterly winds near the radar site. Temperature changes are generally small. The largest change is a warming of 0.3 K or less over the radar in response to the weakened cold air advection. Wind and temperature differences at level 4 (not shown) are very similar to those at level 2. The vertical cross section through the radar location at that time is shown in Figure 12. Compared to the control run, the seabreeze front is weakened and shifted eastward (by approximately 5 km; see also Table 2). By hour 6 of the forecast, which is two hours past the end of the wind assimilation, the beneficial impact of the radar data can now be seen to the west of the radar location (Figure 13), a result of decreased westward advection of easterly momentum. The vertical cross section (Figure 14) shows the center of the seabreeze circulation at $x=30$ km, approximately 5 km east of the control run position (see Table 2). However, the leading edge of the updraft is shifted east by 15 km, resulting in a sharpened seabreeze front. As before, changes in the temperature field are small and are a direct result of the changed advection and adiabatic cooling patterns.

Compared with the verifying PAM data, the wind assimilation results in minor improvements in the wind field and no improvements in the temperature field.

4.4. Wind and temperature assimilation

This run uses the full assimilation scheme between forecast hours 2 and 4 (16 UTC to 18 UTC). TREC and SPRINT winds are used in the objective analysis and potential temperatures are retrieved from the four-dimensional wind fields. The

first guess, analysis, and analysis increment fields at level 2, hour 3 shown in Figure 15 are quite similar to those of the wind-only assimilation run. The analysis increments at level 4, the first level for which a temperature is retrieved, is shown in Figure 16. It is obvious that the retrieval scheme is working properly. Temperature increments are negative inland and positive over water and the immediate coast, thus reducing the water-land temperature contrast at the 600 m level by up to 2 K (recall that the positive temperature bias cannot be corrected by the retrieval scheme).

The forecast fields at the end of the assimilation period show improved wind and temperature fields at level 2 (Figure 17). Compared to PAM data, both the wind field and the temperature contrast (see also Table 2) is in much closer agreement. At level 4 (Figure 18), the effect on the temperature contrast is larger (a 1.4 K reduction), since at that level the model is directly nudged toward retrieved temperatures. The vertical cross section (Figure 19) shows that temperature differences are largest at level 4 and quickly drop off below and above. At lower levels, no temperature retrieval is performed (recall that pressure retrievals are not performed at the lowest or highest level with wind data and that the temperature retrieval requires retrieved pressures at surrounding layers). At upper levels, smaller impacts are related to two separate factors. The first is the amount of data and resulting size of the analysis increments. Even though wind data are assimilated up to 2 km, the data coverage is restricted to a small area around the radar (viz. Figure 2). The second is the smaller east-west temperature gradient in the control run. Forecast errors at upper levels are smaller, with correspondingly smaller effects of data assimilation. The updraft maximum of the seabreeze front in Figure 19 is at $x = -10$ km, some 15 km east of the control run position and close to that indicated by the PAM data (see Table 2). At hour 6 of the forecast, forecast errors have grown somewhat. Both the horizontal cross sections at levels 2 (Figure 20) and level 4 (Figure 21), and the vertical cross section through the radar location (Figure 22), show the updraft maximum to be at $x = -35$ km, almost 20 km too far inland compared to PAM observations (see Table 2). The difference pattern from the control run has been advected with the easterly flow since the end of the assimilation, as was the case with the wind-only assimilation run. The temperature difference fields show a slight weakening and broadening of the gradient between hours 4 and 6. Thus, the beneficial effect of the data

assimilation remains largely intact, indicating that the changes introduced by the nudging are not rejected by the model during the forecast. Even though forecast errors grow after the end of the assimilation, they remain significantly smaller than in either the control or wind-only assimilation runs. The beneficial effects of the temperature retrieval and assimilation are illustrated by a comparison of the difference plots in Figures 20b and 22b (showing differences between the full assimilation and control) with those in Figure 23 (showing differences between the full assimilation and the wind-only assimilation). The temperature difference fields at level 2 are virtually identical, thus the entire improvement in the temperature forecast is due to the temperature assimilation. Wind field differences show a significant additional improvement in the full assimilation over the wind-only assimilation.

5. Summary and conclusions

The real data tests of a single-Doppler radar data assimilation and forecast system have been conducted for a Florida sea breeze case over the Cape Kennedy area (during the CaPE experiment). The model forecast in this case was overpredicting the strength and westward penetration of the Atlantic seabreeze. As was found in earlier experiments with simulated data, assimilation using Newtonian nudging benefits from temperature data in addition to wind data. The thermodynamic retrieval technique was successful in retrieving a horizontal temperature gradient from the radar-derived wind fields that, when assimilated into the model, led to a significantly improved forecast of the seabreeze strength and position. Unlike the Observing System Simulation Experiments reported in Hamill and Nehrkorn (1993), the real data forecast using winds and temperatures was clearly better than either the control or wind-only assimilation forecast, while differences between the wind-only and control runs were comparatively small.

The CaPE case was selected even though there was no convective development along the seabreeze in the Cape Kennedy area that day, because the seabreeze circulation was sampled well by the CP4 radar. Radar scan patterns on other days during CaPE prevented tests of the technique for cases with convective initiation along the seabreeze front.

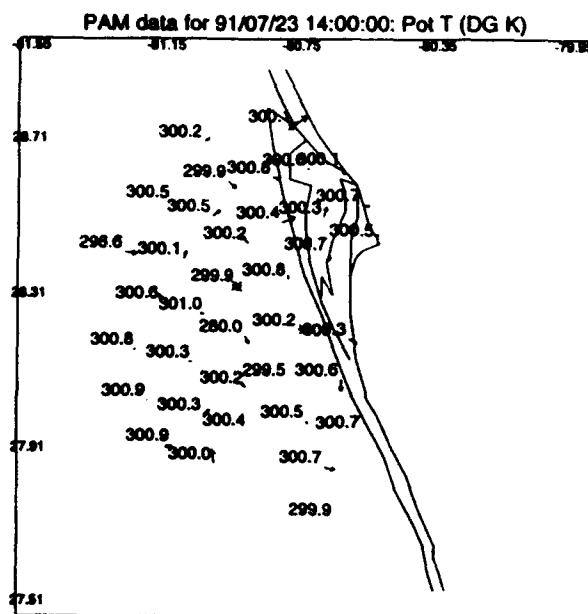
The present study proves the soundness of the approach and feasibility of single Doppler radar data assimilation. However, there are several factors which limit the general applicability of the prototype technique in its present form to thunderstorm forecasting. Because of the requirements for high vertical and temporal resolution and good areal coverage of the radar data in the boundary layer, this technique will only work if sufficient scatterers are present and if appropriate radar scan patterns are used. A potentially more serious limitation is that boundary layer convergence features (such as the seabreeze front) that can be predicted by the simple prototype mesoscale model used in this study do not account for all or even the majority of significant convective developments. More typically, synoptic scale fronts, or mesoscale features of those fronts and interactions of outflows from decaying cells with each other, or with other convergence lines such as the seabreeze front, are responsible for convective initiation. Modeling these complex scale interactions is a challenging problem for which more sophisticated models are needed.

6. References

- Cotton, W. R., R. McAnelly, C. Tremback and R. Walko, 1989: A dynamic model for forecasting new cloud development. AFGL-TR-89-0011. Air Force Geophysics Laboratory, Hanscom AFB, MA. 81 pp. [NTIS ADA213939]
- Cressman, G., 1959: An operational objective analysis system. *Mon. Wea. Rev.*, **87**, 367-374.
- Gal-Chen, T., 1986: Selected comments on the use of the divergence equation to obtain temperature and geopotentials from an observed wind. *J. Atmos. Ocean. Technol.*, **3**, 730-733.
- Gustafson, G. B., J.-L. Moncet, C. F. Ivaldi, H.-C. Huang and J. M. Sparrow, 1991: Mesoscale prediction and satellite cloud analysis for advanced meteorological processing systems. PL-TR-91-2008. Phillips Laboratory, Geophysics Directorate, Hanscom AFB, MA. 112 pp. [NTIS ADA 240510]
- Hamill, T. M., 1992: Prediction of thunderstorm initiation through 4-dimensional data assimilation of doppler radar data. PL-TR-92-2029. Phillips Laboratory, Directorate of Geophysics, Hanscom AFB, MA. 86 pp, ADA251243.

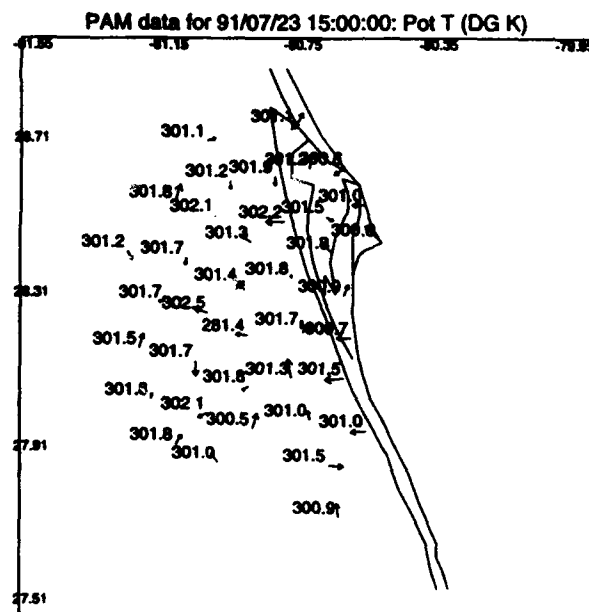
- Hamill, T. M. and T. Nehrkorn, 1993: Sensitivity Testing of a single-Doppler temperature retrieval and forecast system. PL-TR-93-2071. Phillips Lab., Directorate of Geophysics, Hanscom AFB, MA. 86 pp, ADA267278.
- Kropfli, R. A., 1986: Single Doppler radar measurements of turbulence profiles in the convective boundary layer. *J. Atmos. Ocean. Technol.*, 3, 305-314.
- Liou, Y.-C., 1989: Retrieval of Three-Dimensional Wind and Temperature Fields from one Component Wind Data by using the Four-Dimensional Data Assimilation Technique. M.S. Thesis, University of Oklahoma, Norman, OK, 112 pp.
- Mohr, C. G., L. J. Miller, R. L. Vaughan and H. W. Frank, 1986: The merger of mesoscale data sets into a common cartesian format for efficient systematic analyses. *J. Atmos. Ocean. Technol.*, 3, 143-161.
- Pielke, R. A., 1984: Mesoscale meteorological modeling. Academic Press, Orlando, FL. 612 pp.
- Stauffer, D. R. and N. L. Seaman, 1990: Use of four-dimensional data assimilation in a limited-area mesoscale model. Part I: Experiments with synoptic-scale data. *Mon. Wea. Rev.*, 118, 1250-1277.
- Tripoli, G. J. and W. R. Cotton, 1982: The Colorado State University Three-Dimensional Cloud / Mesoscale Model - 1982; Part I: General Theoretical Framework and Sensitivity Experiments. *J. Rech. Atmos.*, 16, 185-219.
- Tuttle, J. and G. B. Foote, 1990: Determination of the boundary layer airflow from a single Doppler radar. *J. Atmos. Ocean. Tech.*, 7, 218-232.
- Vemuri, V. and W. J. Karplus, 1981: *Digital Computer Treatment of Partial Differential Equations*. Prentice Hall, Inc., Englewood Cliffs, NJ. 449 pp.
- Williams, S. F., K. Caesar and K. Southwick, 1992: The convection and precipitation electrification (CaPE) operations summary and data inventory. National Center for Atmospheric Research, Office of Field Project Support, Boulder, CO. 425 pp.
- Wilson, J. W. and W. E. Schreiber, 1986: Initiation of convective storms at radar-observed convergence lines. *Mon. Wea. Rev.*, 114, 2516-2536.

a



5 m/s scale: →

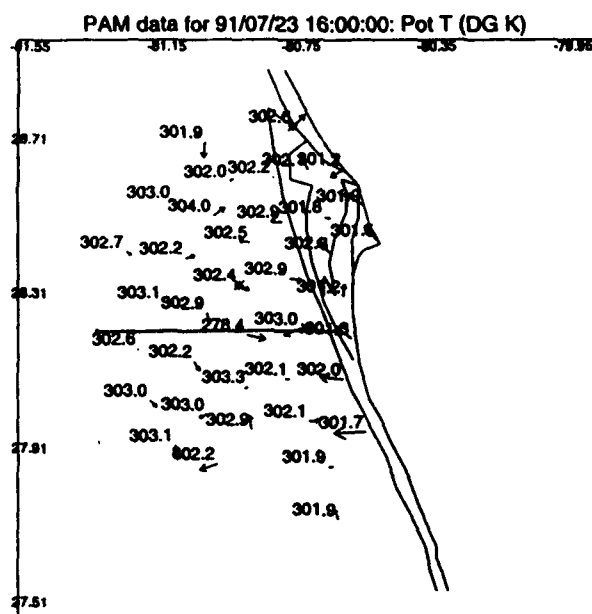
b



5 m/s scale: →

Figure 1: Plots of PAM surface data. Station locations correspond to the origin of the wind vectors; potential temperature is plotted above and to the left of the station location. Position of radars is indicated by asterisks.

c



d

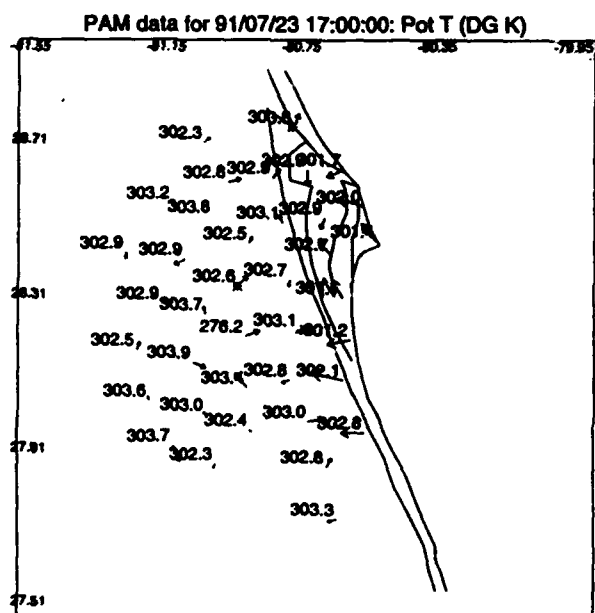
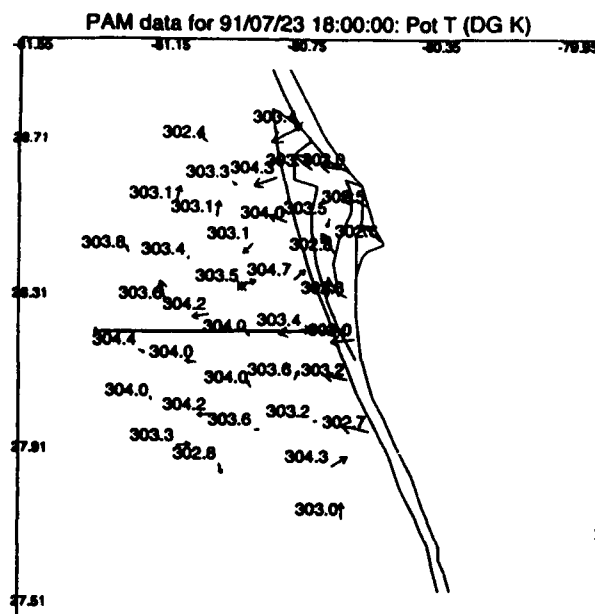


Figure 1 (continued).

e



f

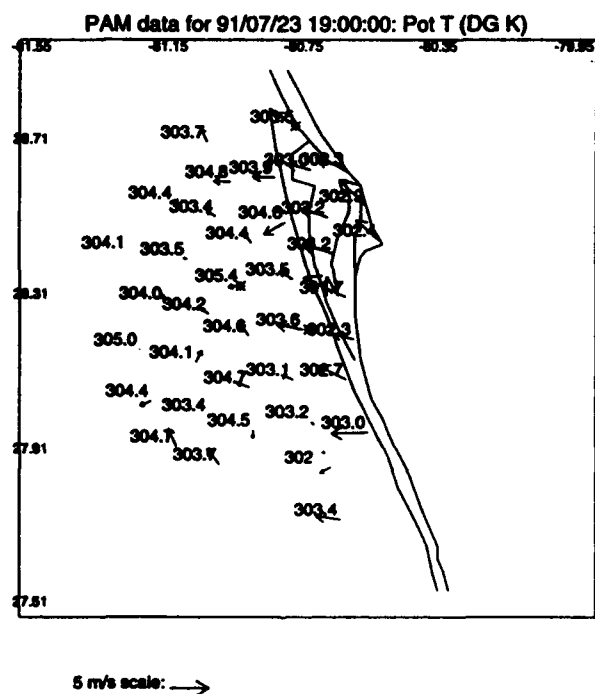


Figure 1 (continued).

g

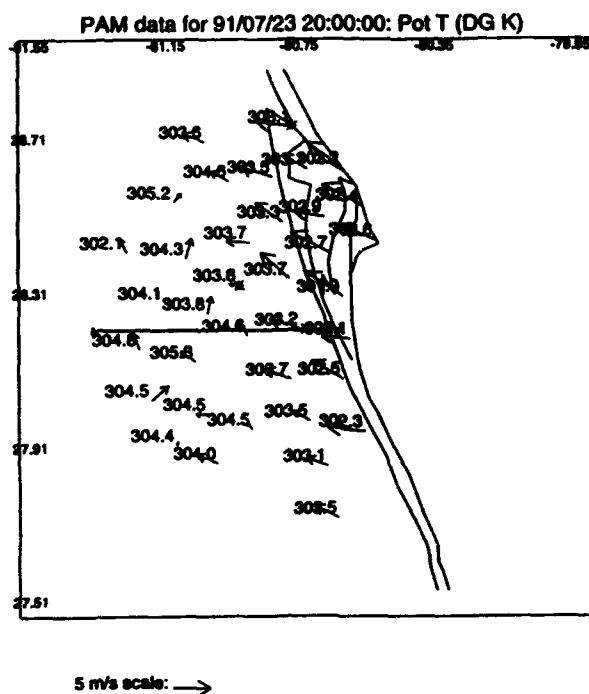
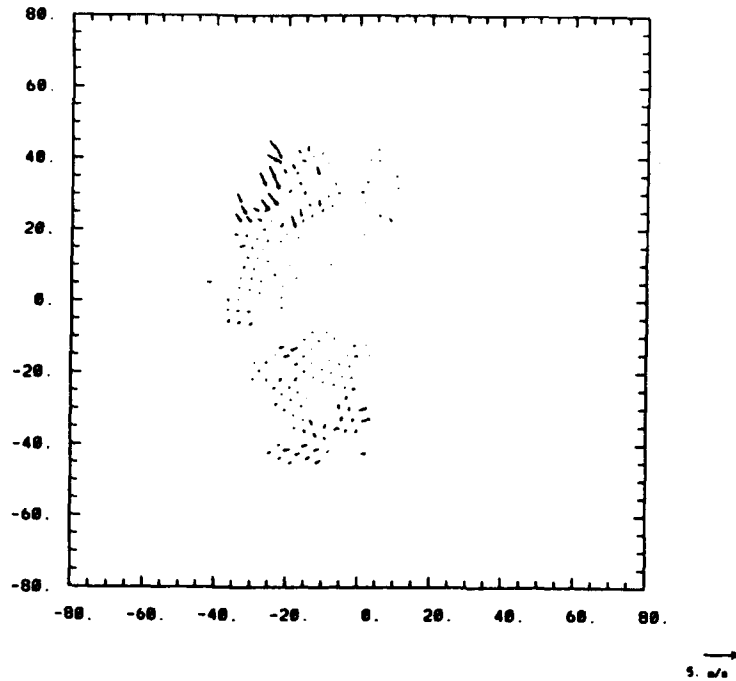


Figure 1 (continued).

TREC VEL VECTORS (WITH QC)
 165916 TO 170603 EL= 0.3 910723
 CORMIN,CORMAX,THRVAR,THRVD,SRAD,ARSIZ= 0.40 1.50 25.0 1.0 4.0 7.0

a



TREC VEL VECTORS (WITH QC)
 165940 TO 170627 EL= 0.9 910723
 CORMIN,CORMAX,THRVAR,THRVD,SRAD,ARSIZ= 0.40 1.50 25.0 1.0 4.0 7.0

b

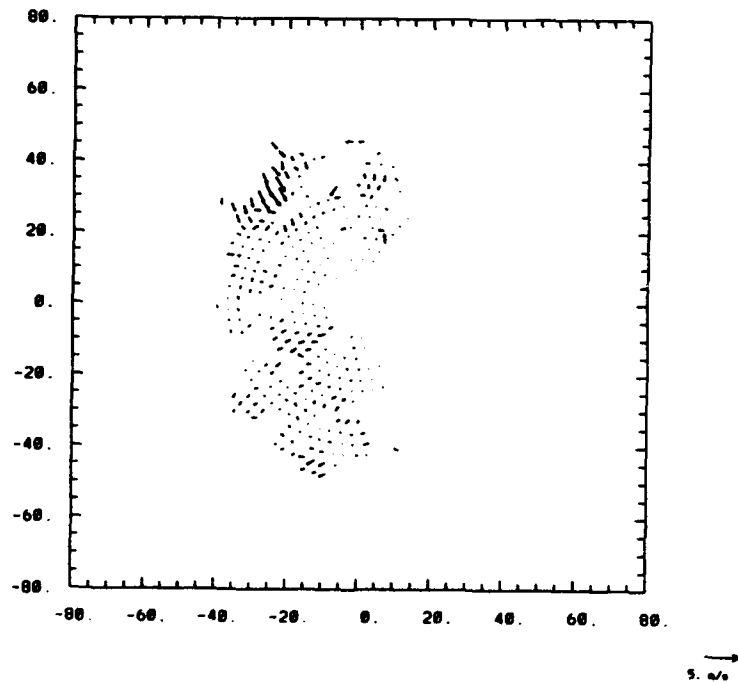
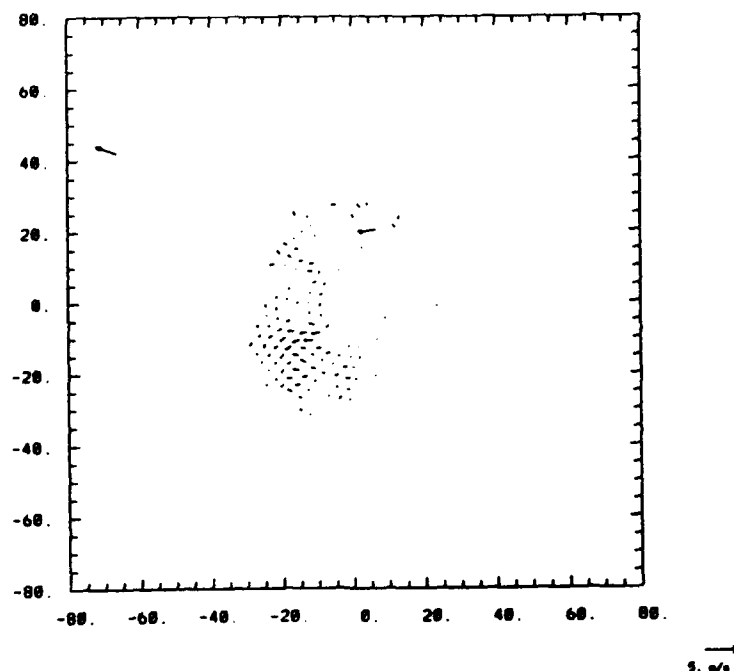


Figure 2: TREC derived winds valid for 1705 UTC, over the same geographic region and with the same wind vector scale as in Figure 1, for elevation angles 0.3°, 0.9°, 1.5°, and 2.1°. (CP4)

TREC VEL VECTORS (WITH QC)
 170005 TO 170651 EL= 1.5 910723
 CORMIN, CORMAX, THRVAR, THRVDF, SRAD, ARSIZ= 0.40 1.50 25.0 1.0 4.0 7.0



TREC VEL VECTORS (WITH QC)
 170029 TO 170715 EL= 2.1 910723
 CORMIN, CORMAX, THRVAR, THRVDF, SRAD, ARSIZ= 0.40 1.50 25.0 1.0 4.0 7.0

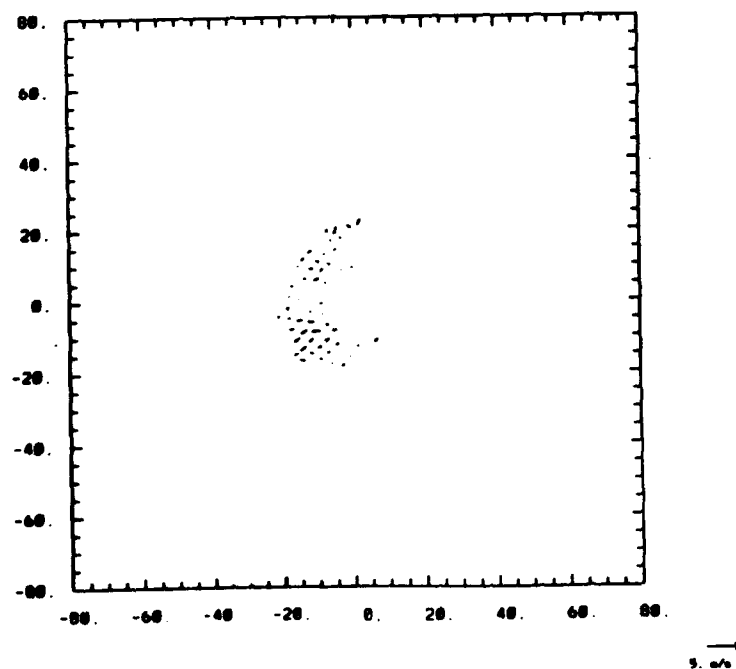


Figure 2 (continued).

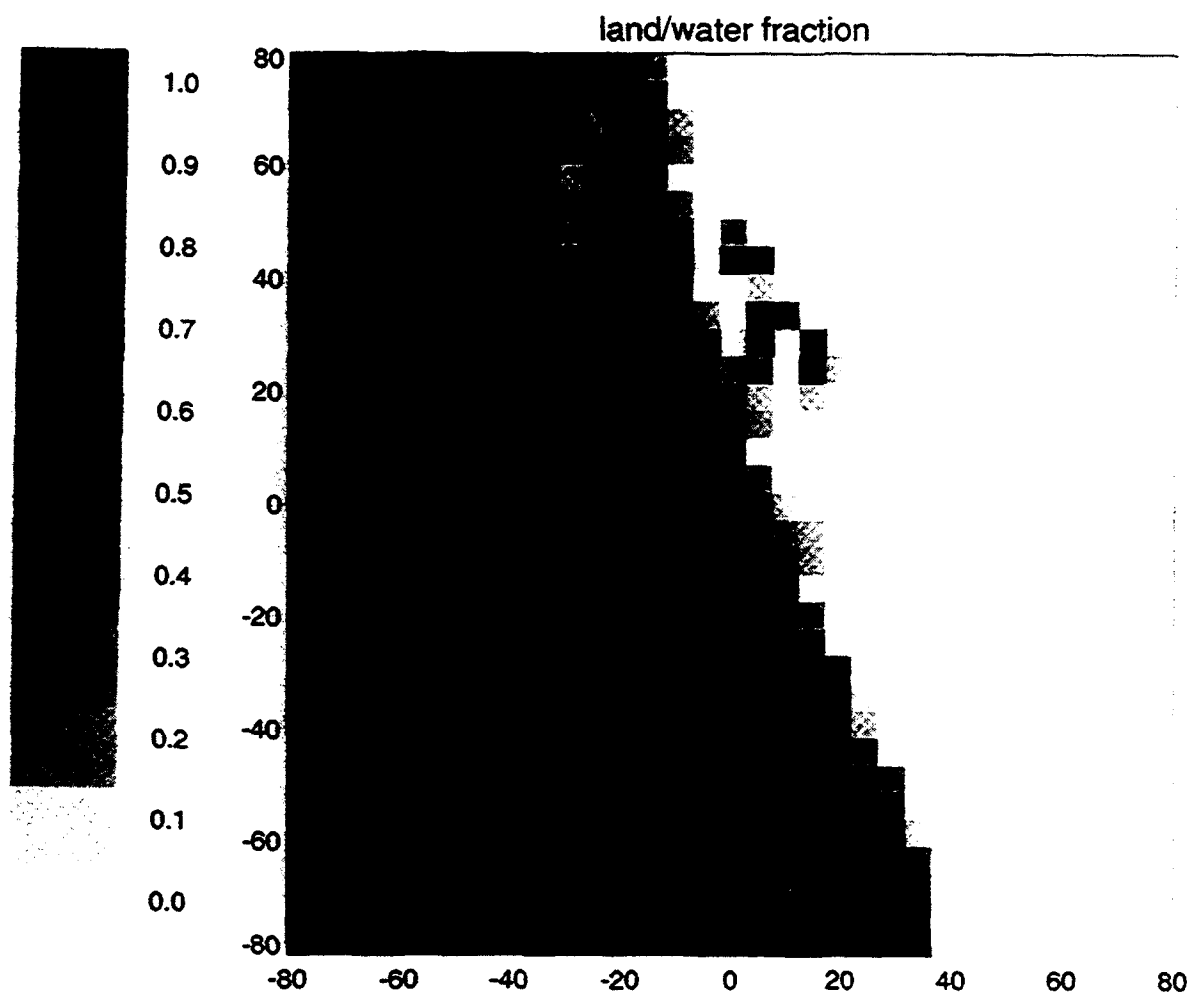
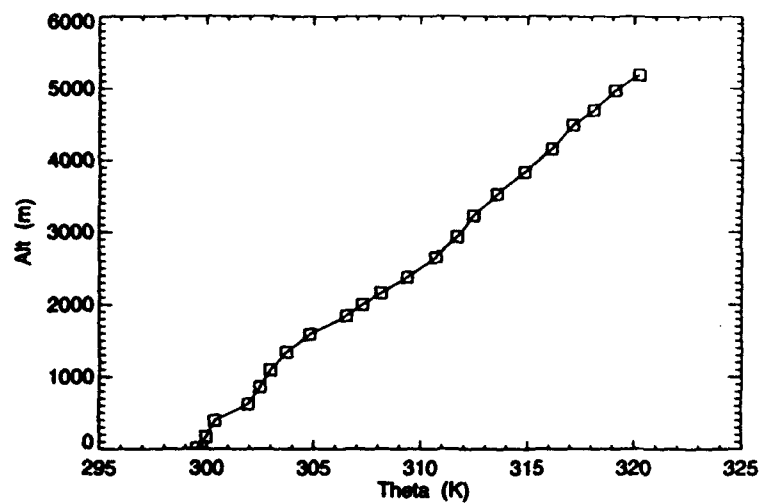


Figure 3: Fractional area of PL-3D gridpoints covered by water. Model domain shown corresponds to the area plotted in Figure 1.

a



b

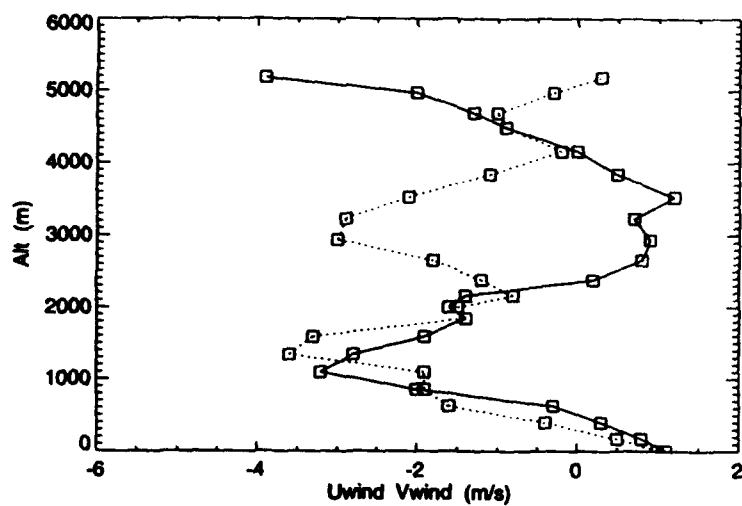


Figure 4: The sounding used to initialize the model runs: potential temperature - top panel; u (solid) and v (dotted) - bottom panel.

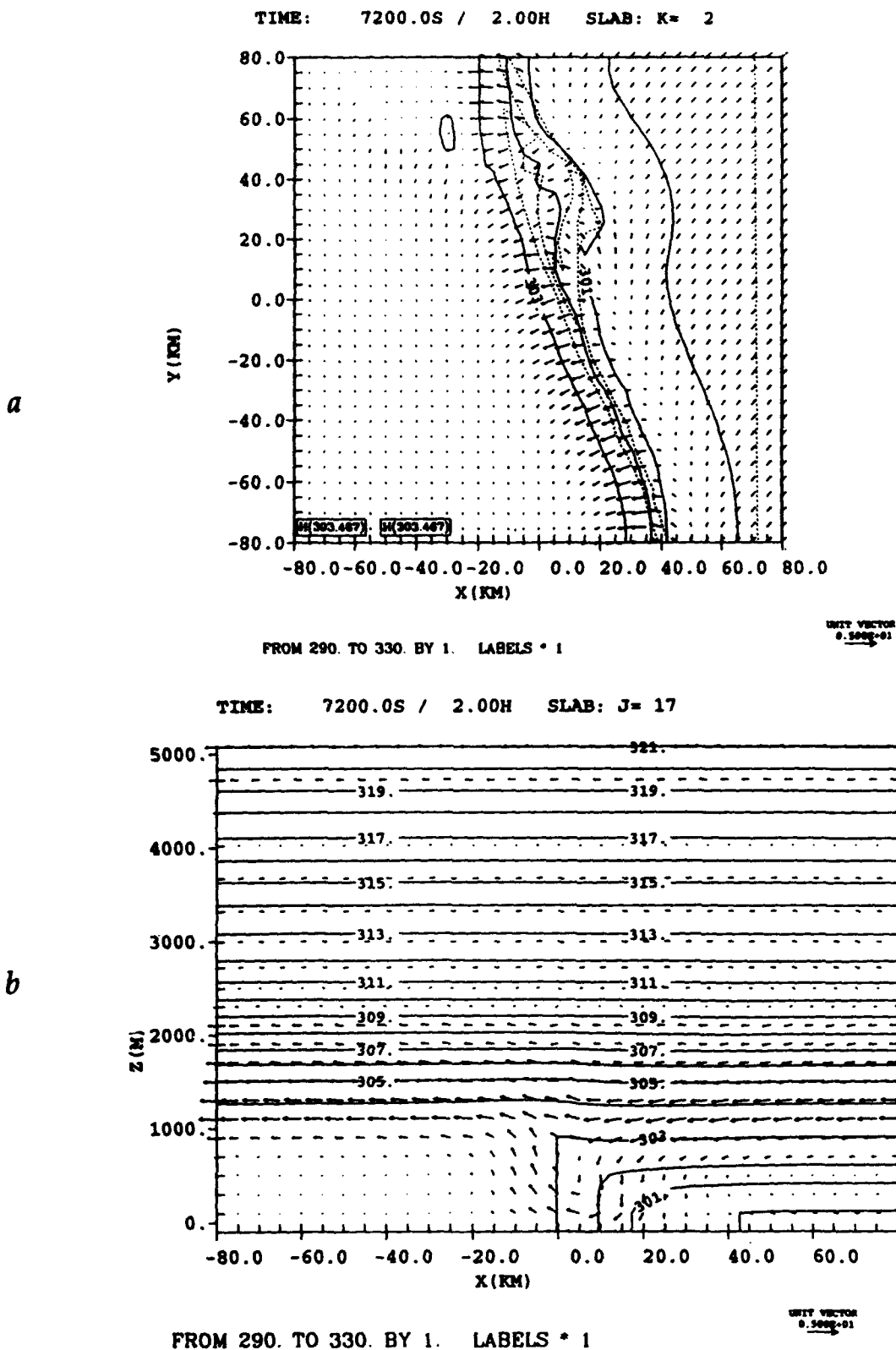
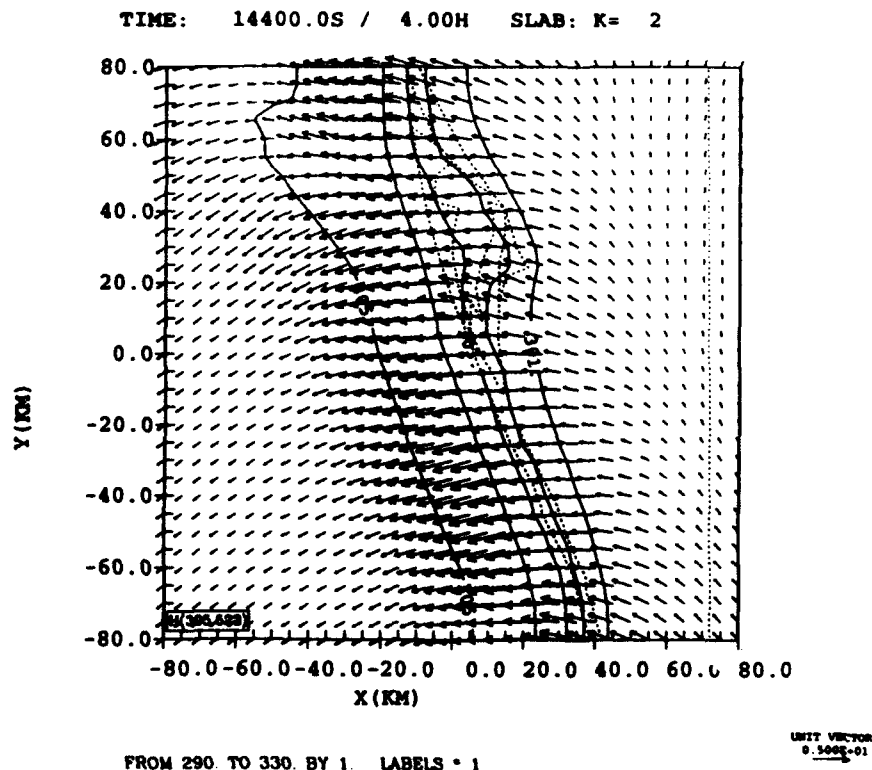


Figure 5: Horizontal cross section of winds and θ at level 2, and vertical cross section at $y=0$, for hour 2 (16 UTC) of the control run. Dotted line in horizontal cross section denotes the coastline. The vector scale is given in m/s.

a



b

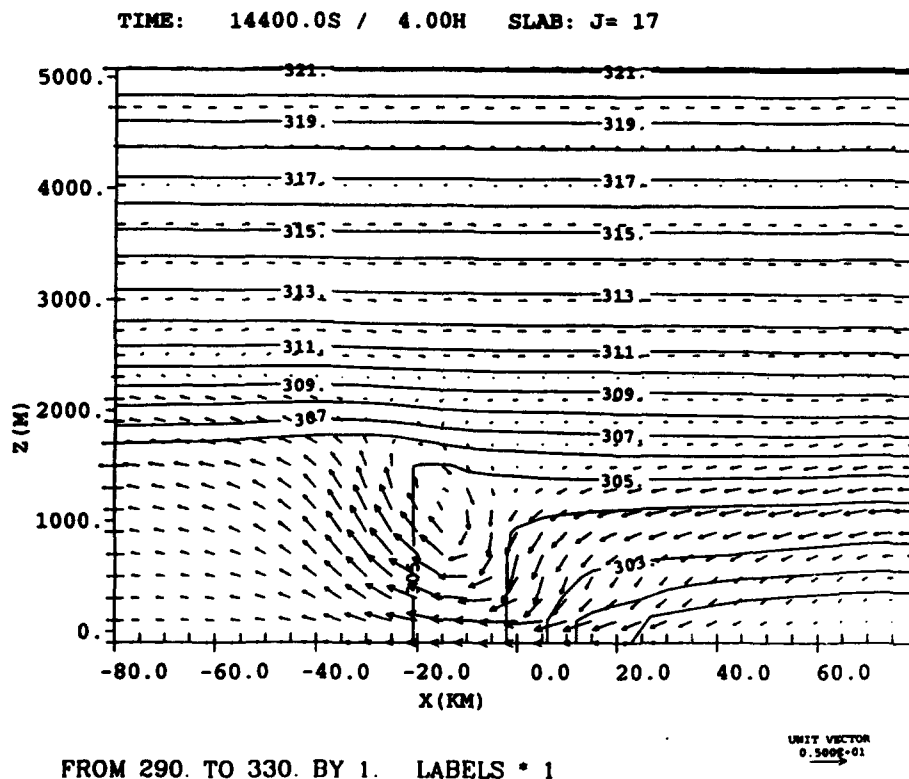


Figure 6: Horizontal cross section of winds and θ at level 2, and vertical cross section at $y=0$, for hour 4 (18 UTC) of the control run. Dotted line in horizontal cross section denotes the coastline. The vector scale is given in m/s.

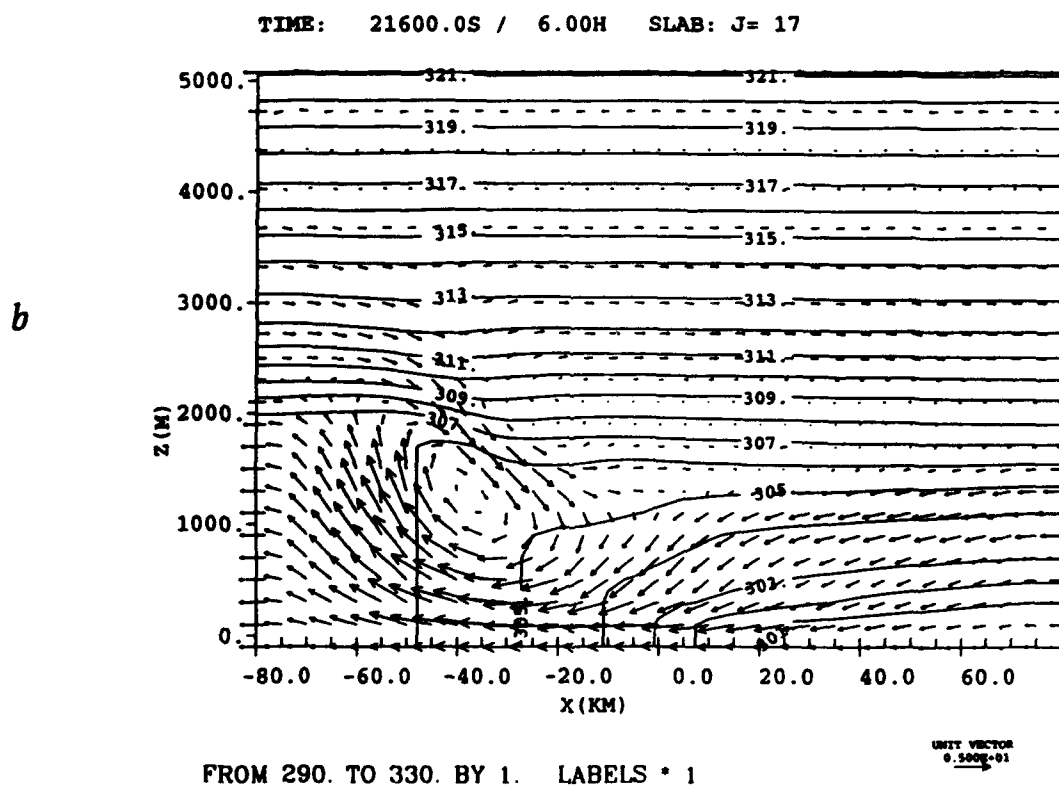
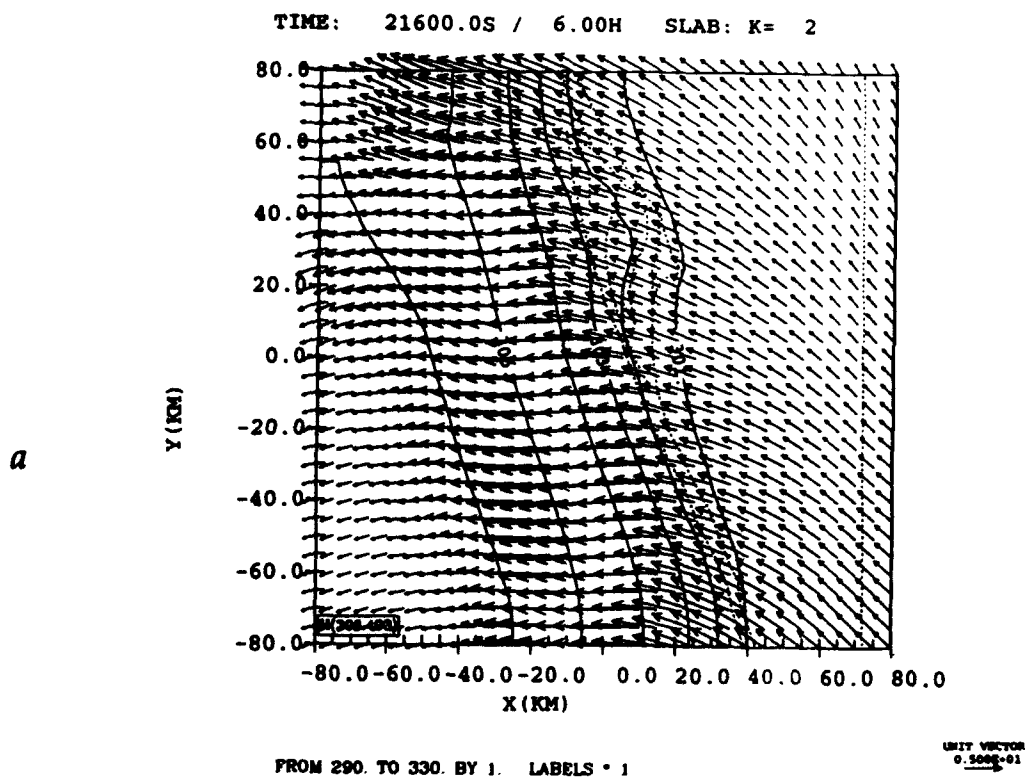
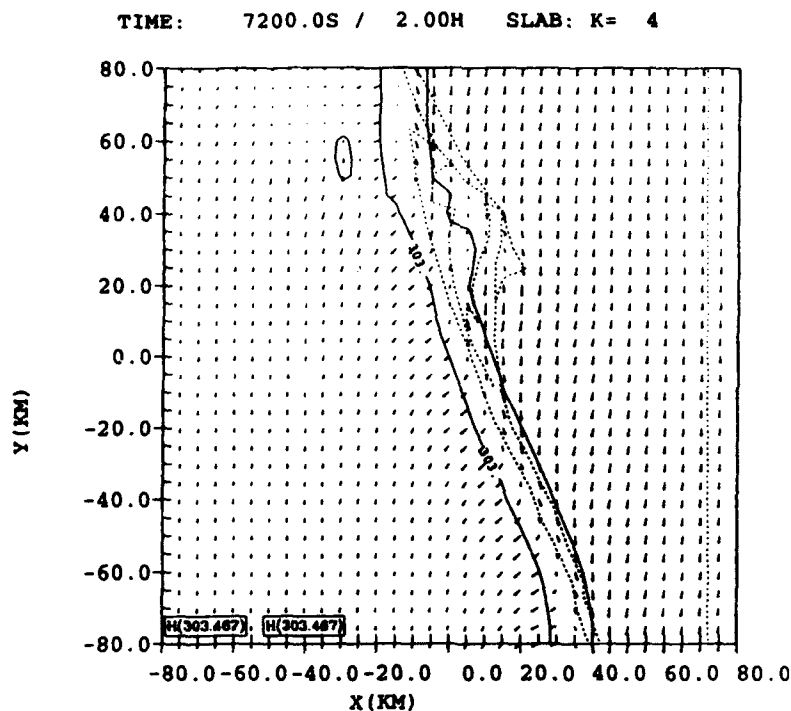


Figure 7: Horizontal cross section of winds and θ at level 2, and vertical cross section at $y=0$, for hour 6 (20 UTC) of the control run. Dotted line in horizontal cross section denotes the coastline. The vector scale is given in m/s.

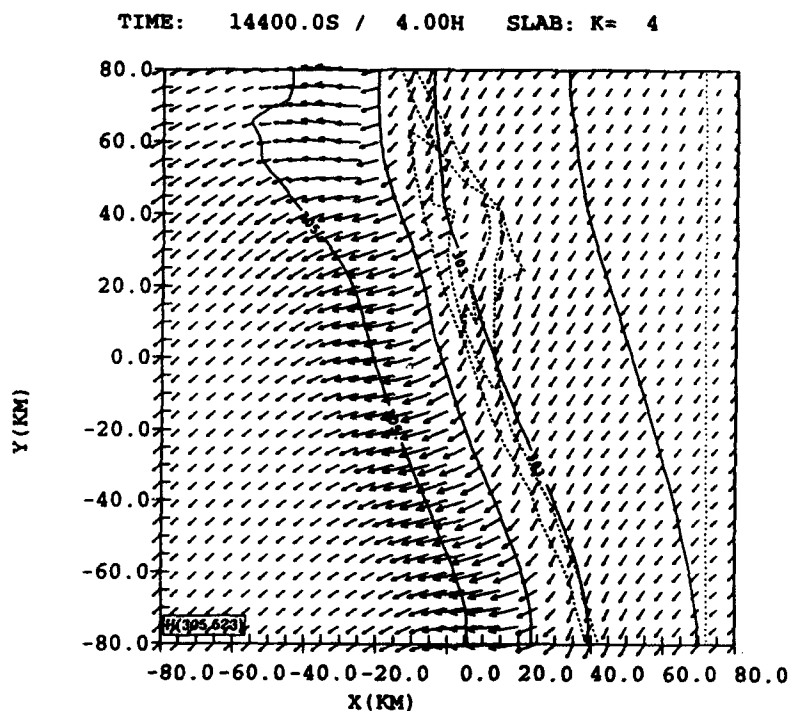
a



FROM 290. TO 330 BY 1 LABELS * 1

UNIT VECTOR
0.500E+01

b



FROM 290. TO 330 BY 1 LABELS * 1

UNIT VECTOR
0.500E+01

Figure 8: Horizontal cross sections of winds and θ at level 4 for hours 2, 4, and 6 (16, 18, and 20 UTC) of the control run. Dotted line denotes the coastline. The vector scale is given in m/s.

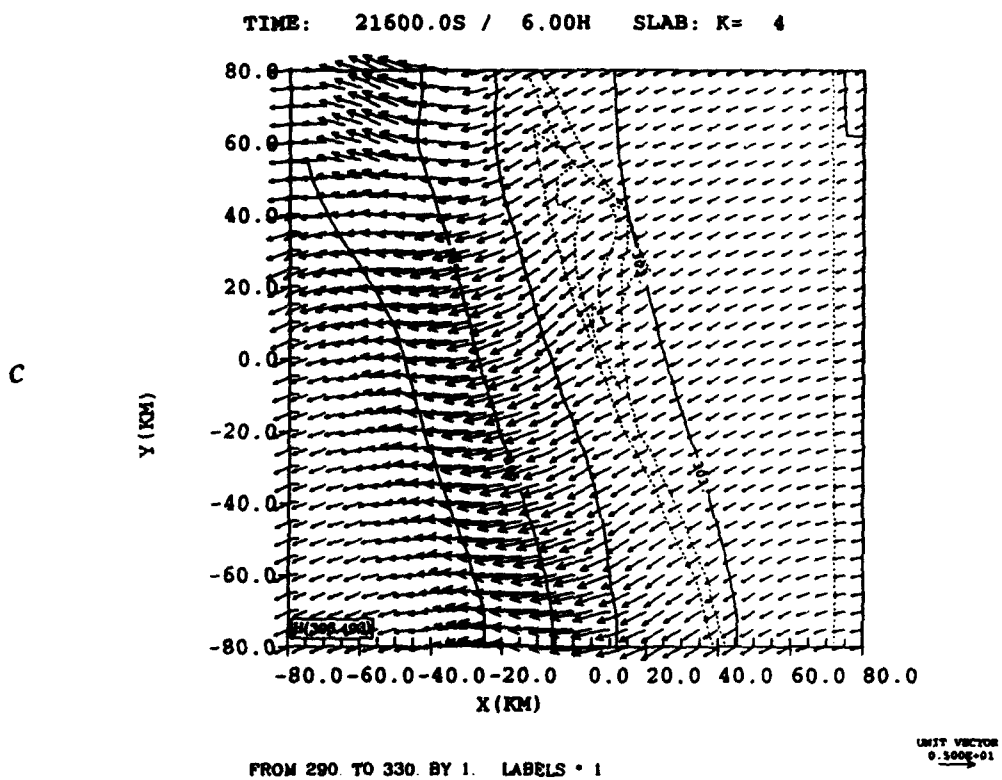


Figure 8 (continued).

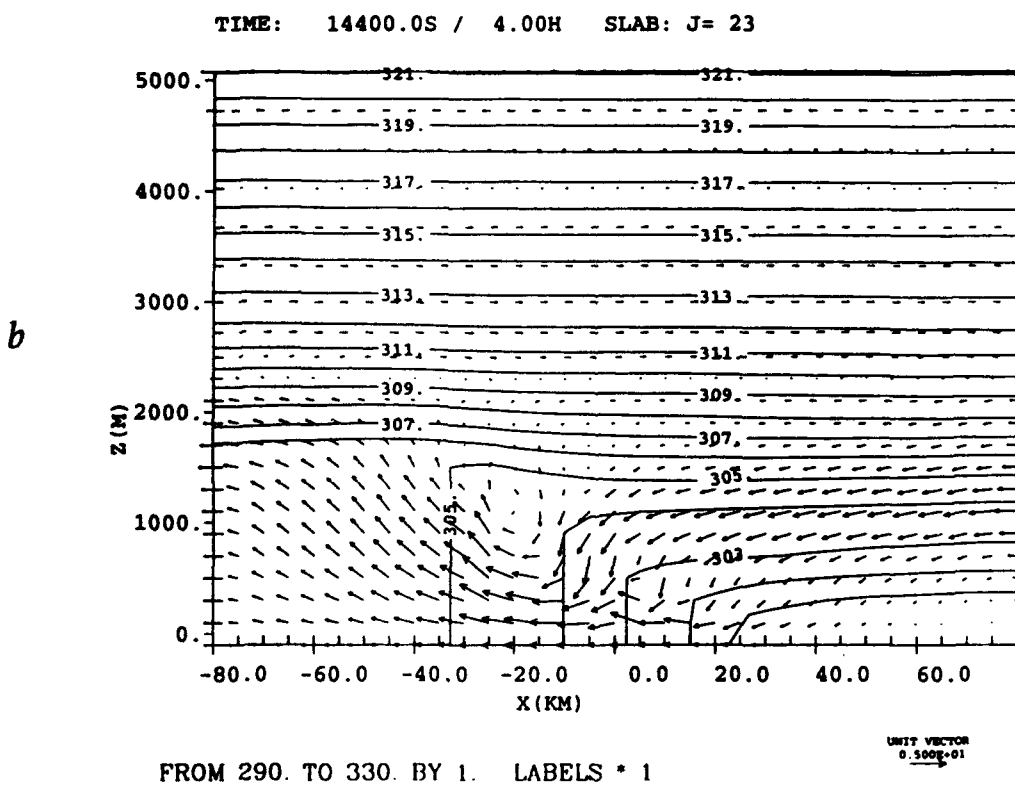
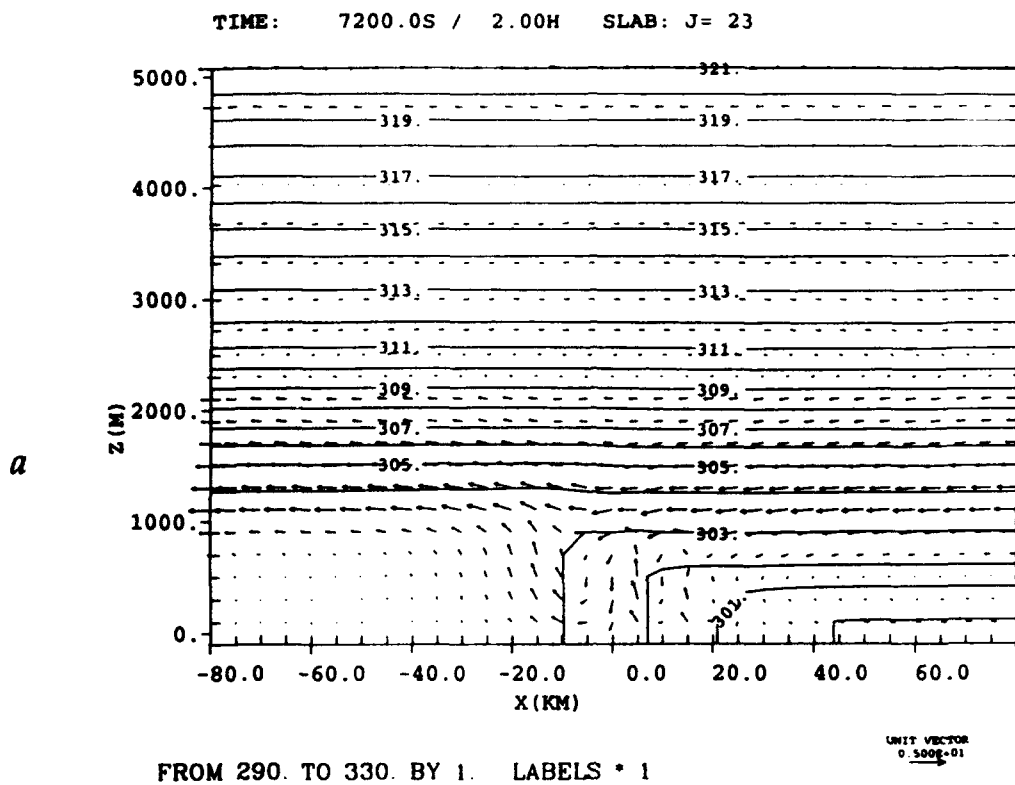
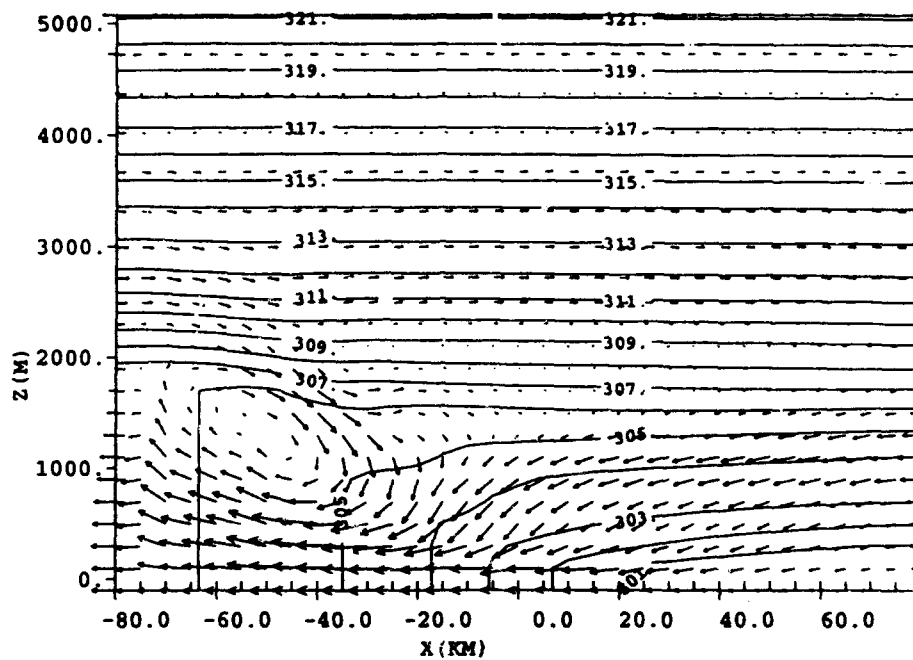


Figure 9: Vertical cross section of winds and θ at $y=+25$ km, for hours 2, 4, and 6 of the control run.

TIME: 21600.0S / 6.00H SLAB: J= 23

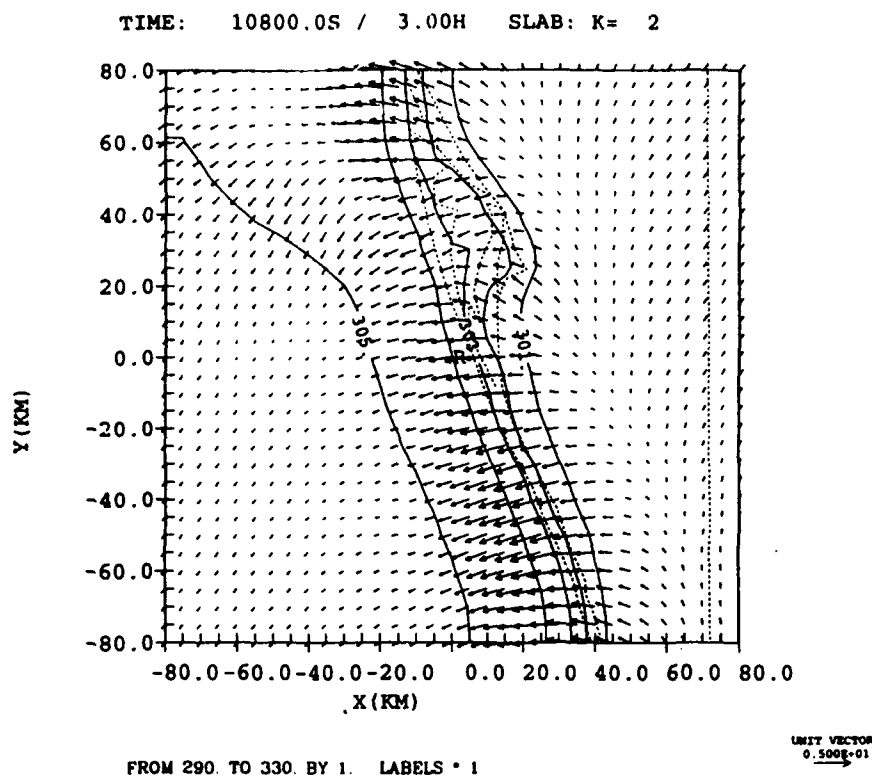
C



FROM 290. TO 330. BY 1. LABELS * 1

Figure 9 (continued).

a



b

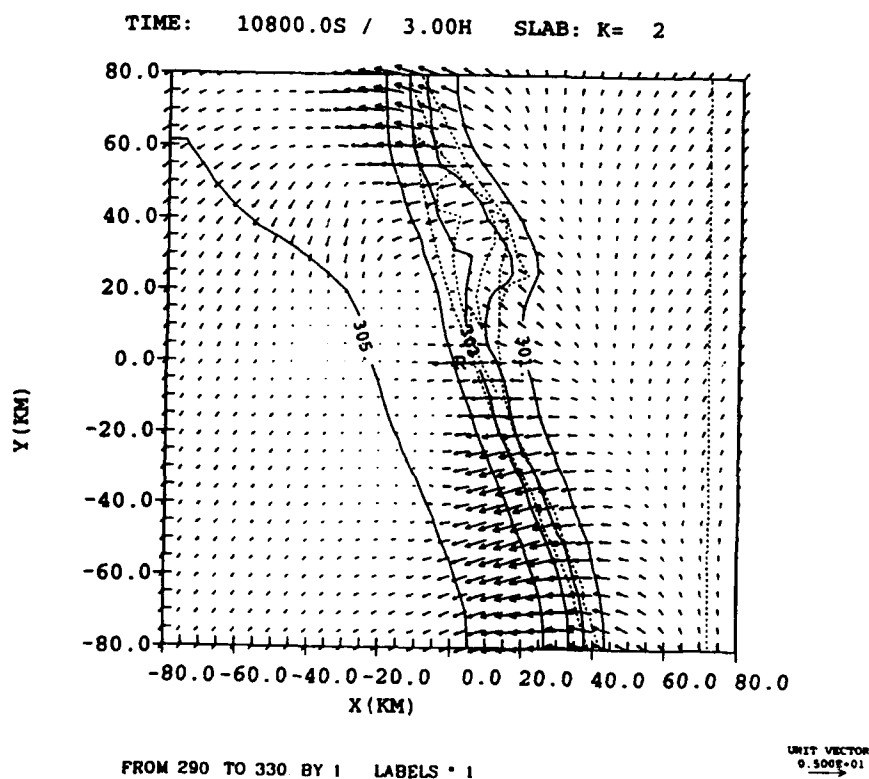


Figure 10: Horizontal cross section of winds and θ at level 2 for hour 3 (17 UTC) of the wind-only assimilation: first guess, analysis, and analysis increments. Dotted line denotes the coastline. The vector scale is given in m/s. The CP4 radar location is shown as the symbol "R".

C

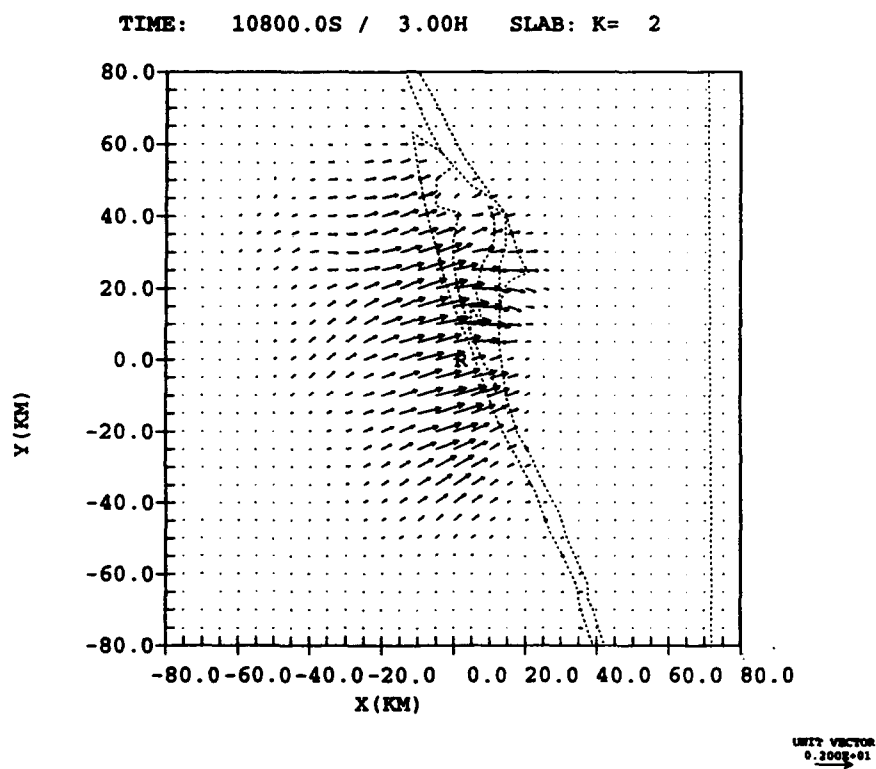
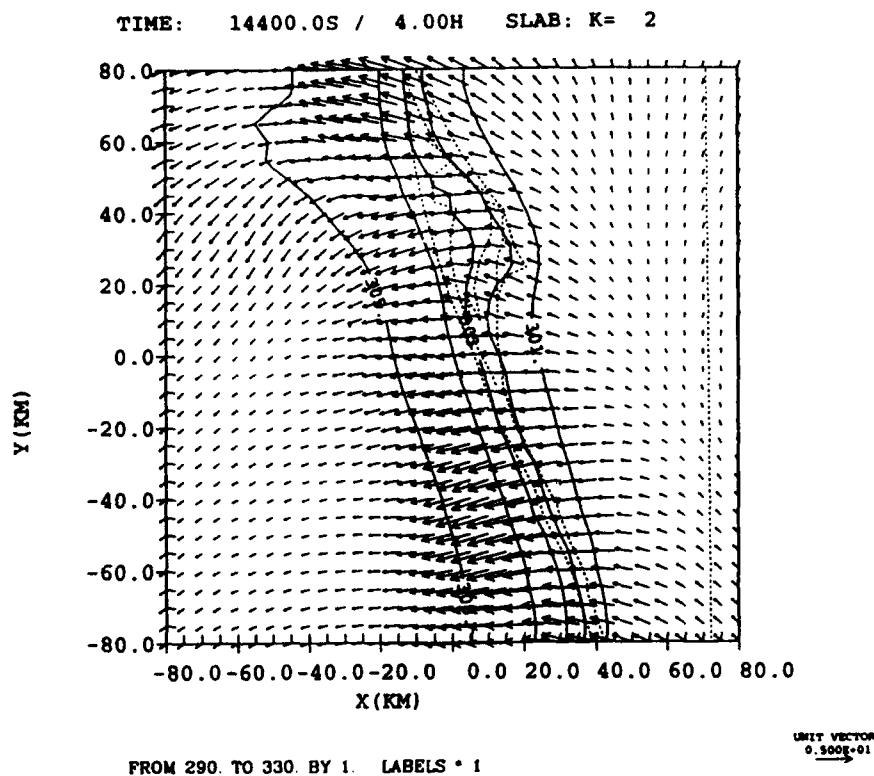


Figure 10 (continued).

a



b

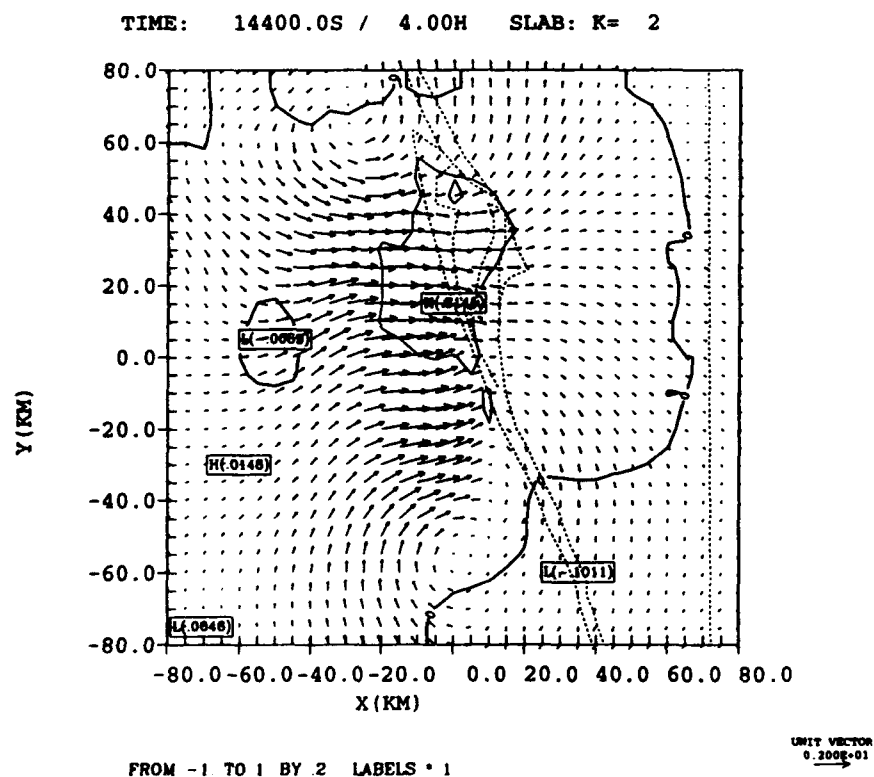


Figure 11: Horizontal cross section of winds and θ for level 2 at hour 4 (18 UTC): wind-only assimilation; and differences from control. Dotted line denotes the coastline. The vector scale is given in m/s.

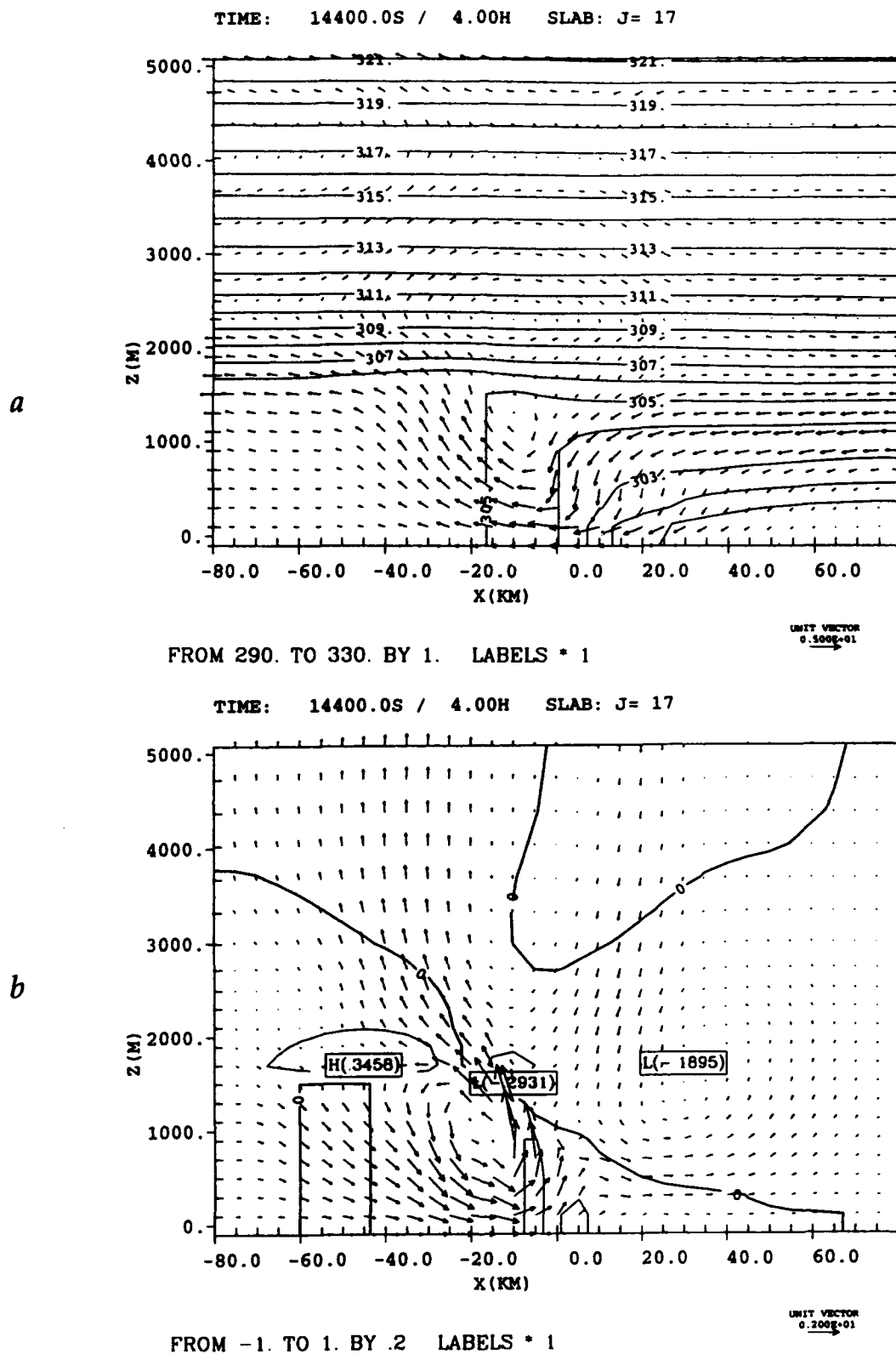
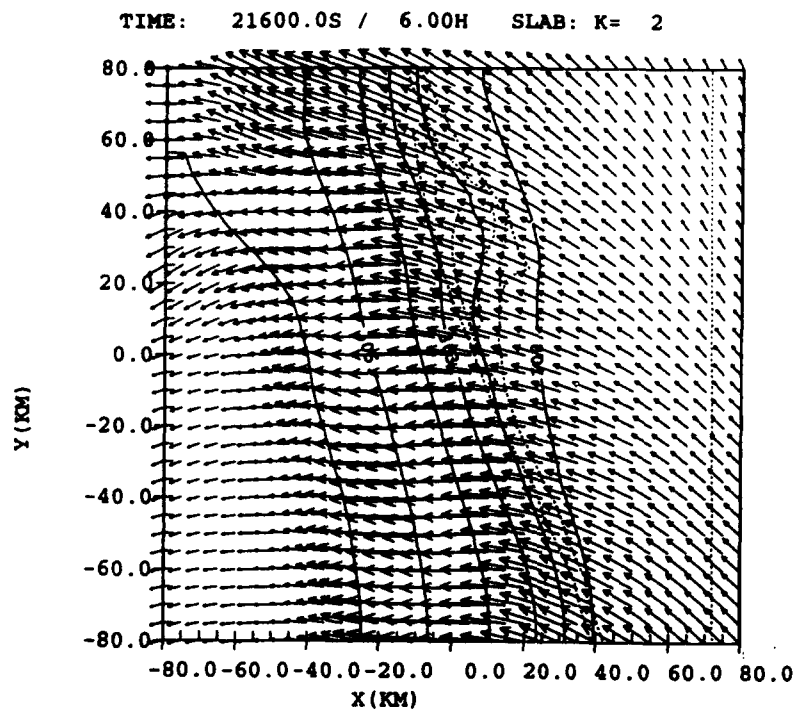


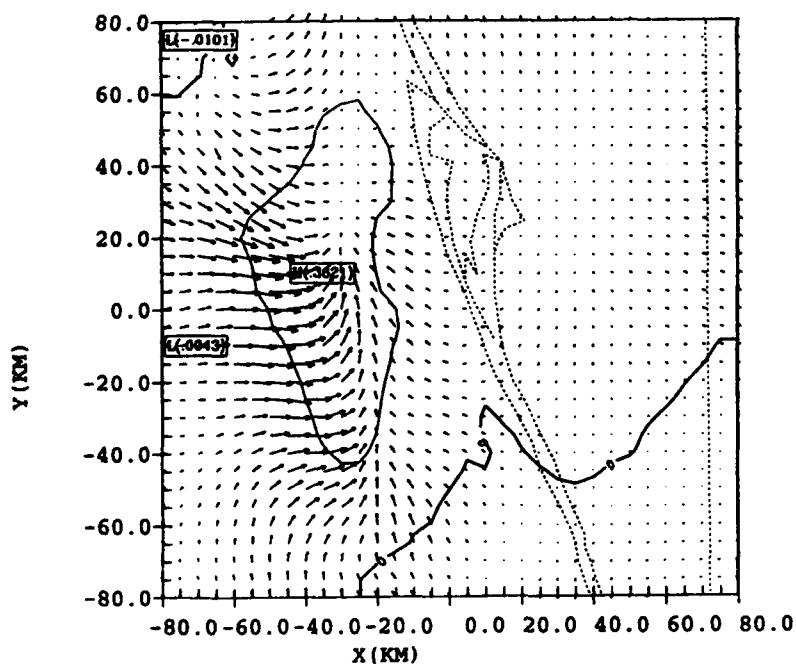
Figure 12: Vertical cross section of winds and θ at $y=0$ for hour 4 (18 UTC): wind-only assimilation; and differences from control.



FROM 290. TO 330. BY 1. LABELS * 1

UNIT VECTOR
0.500E+01

TIME: 21600.0S / 6.00H SLAB: K= 2



FROM -1 TO 1 BY 2 LABELS * 1

UNIT VECTOR
0.200E+01

Figure 13: Horizontal cross section of winds and θ at level 2 for hour 6 (20 UTC): wind-only assimilation; and differences from control. Dotted line denotes the coastline. The vector scale is given in m/s.

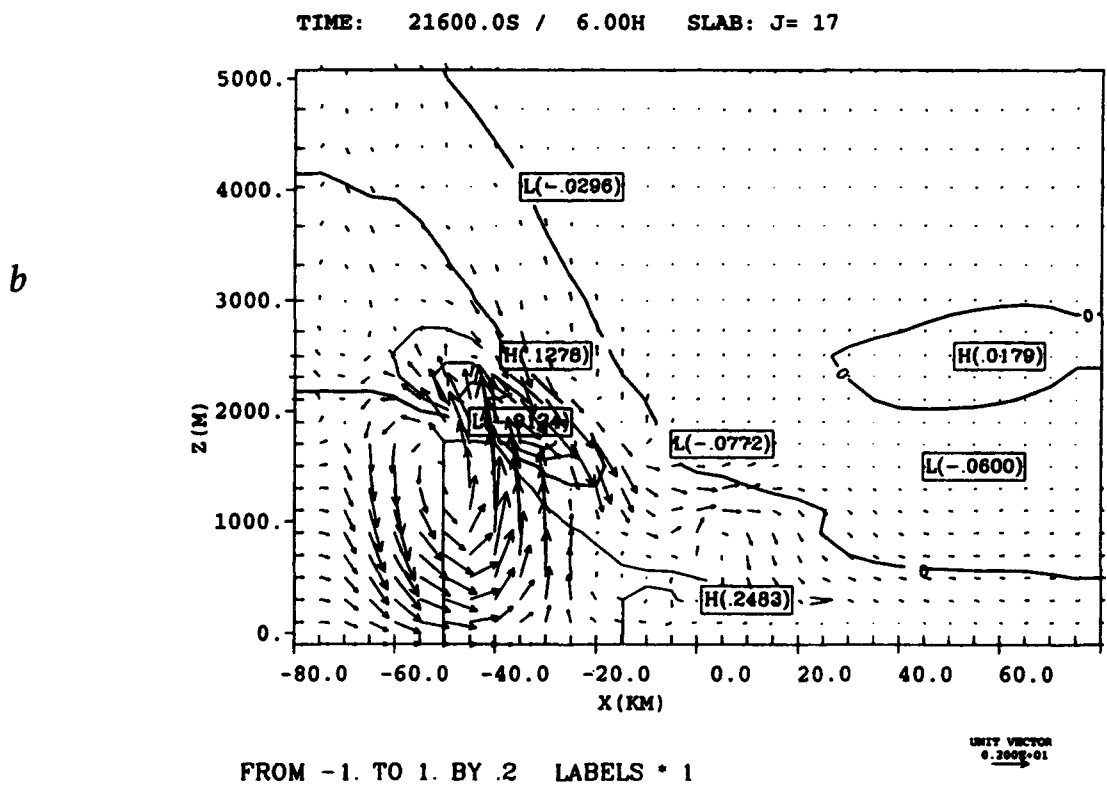
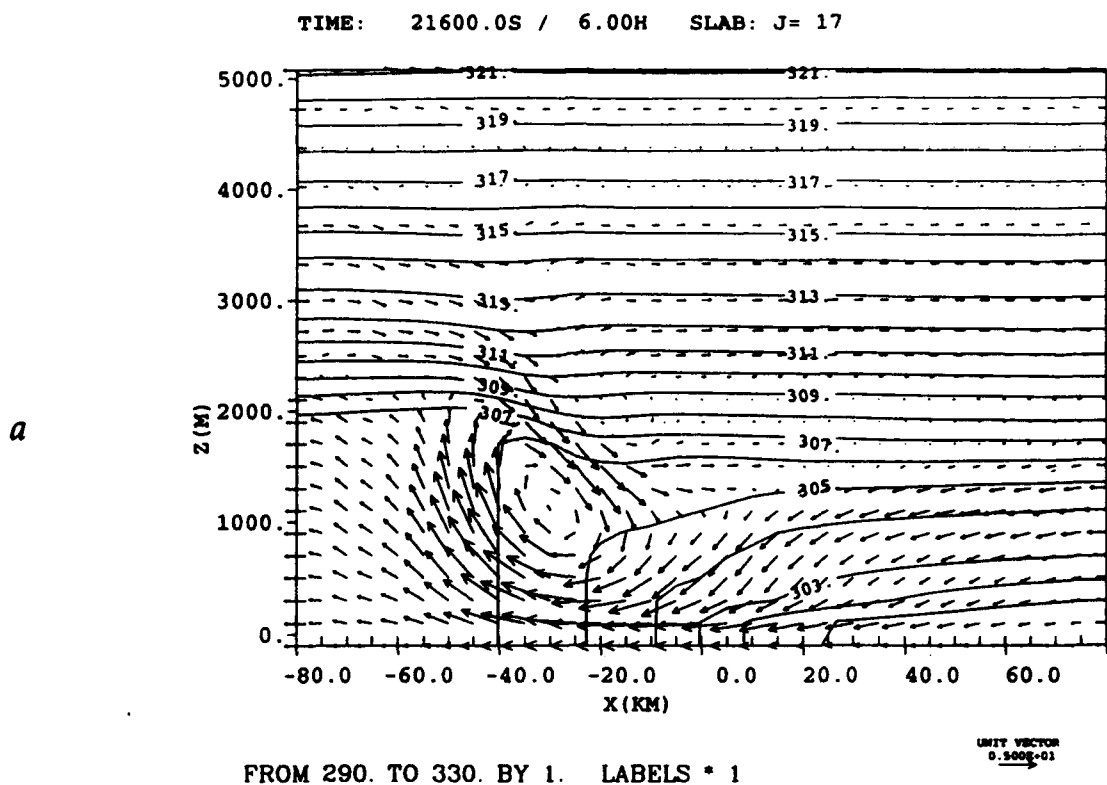


Figure 14: Vertical cross section of winds and θ at $y=0$ for hour 6 (20 UTC): wind-only assimilation; and differences from control.

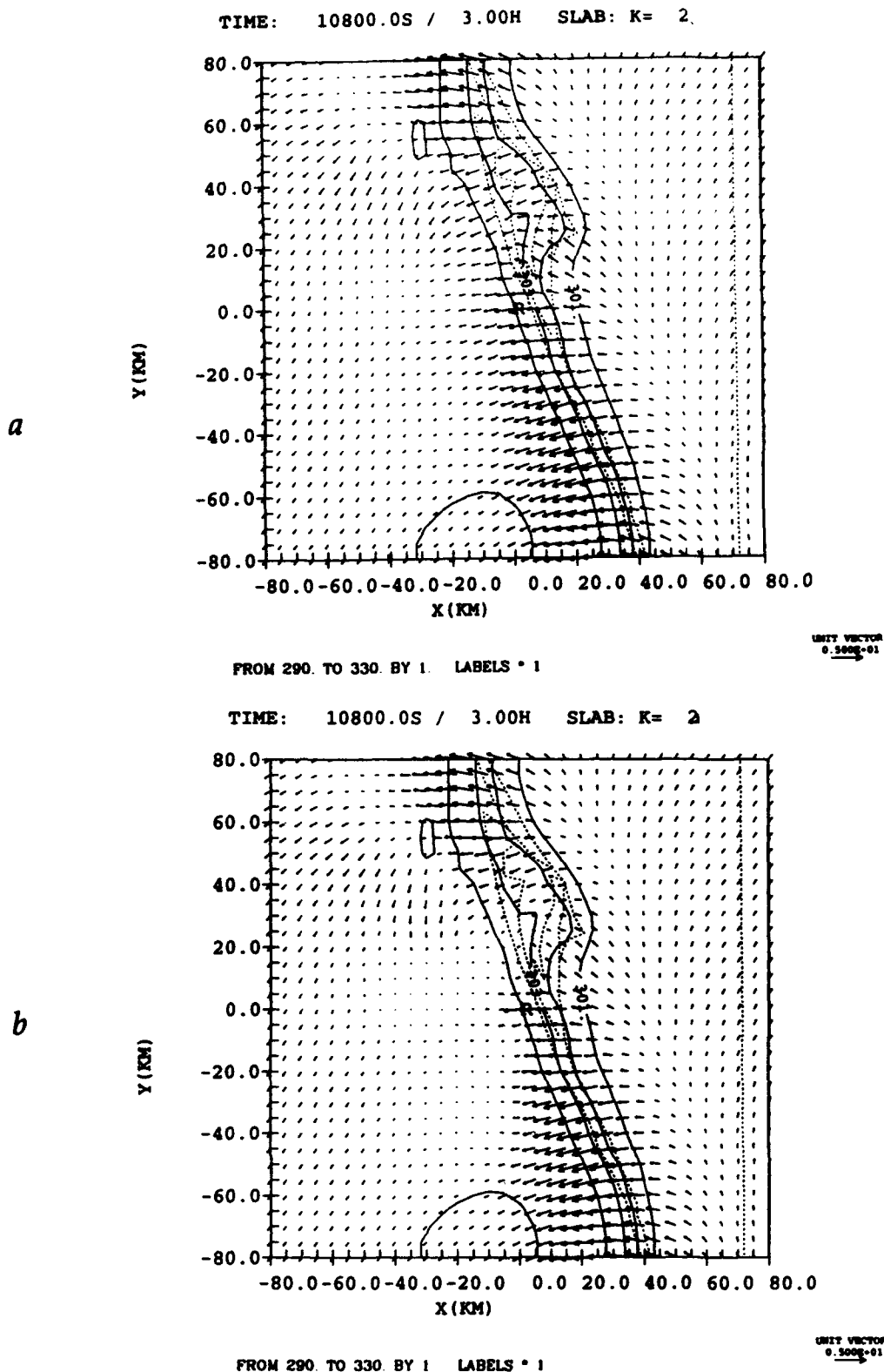


Figure 15: Horizontal cross section of winds and θ at level 2 for hour 3 (17 UTC) of the full assimilation: first guess, analysis, and analysis increments. Dotted line denotes the coastline. The vector scale is given in m/s. The CP4 radar location is shown as the symbol "R".

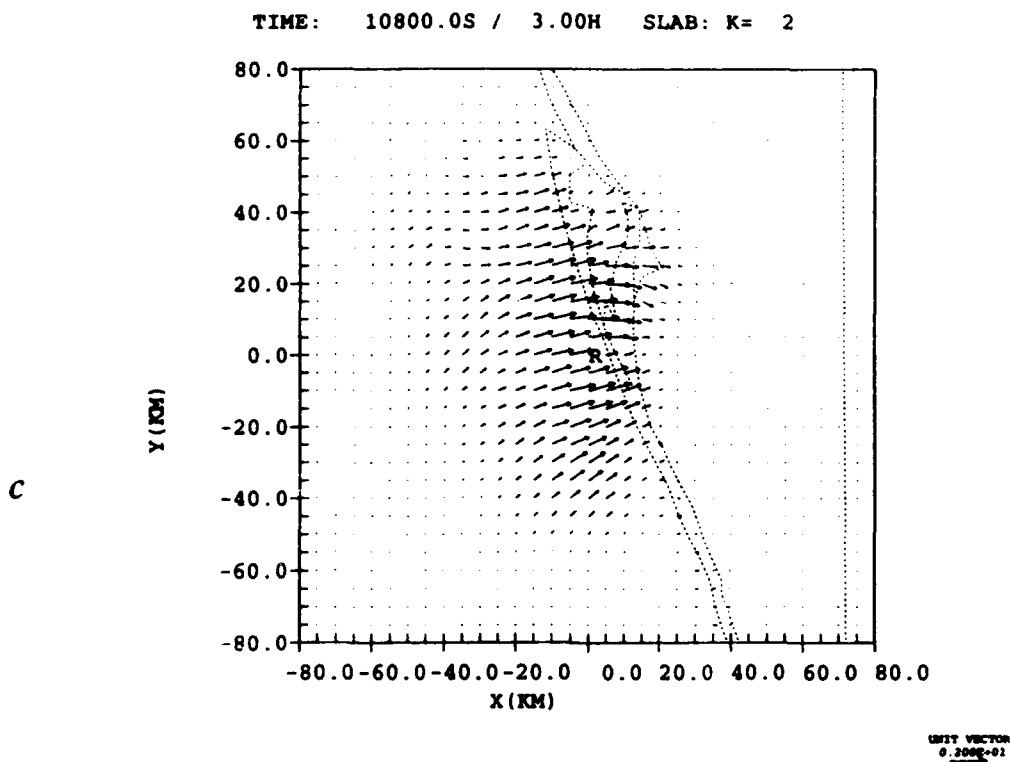


Figure 15 (continued).

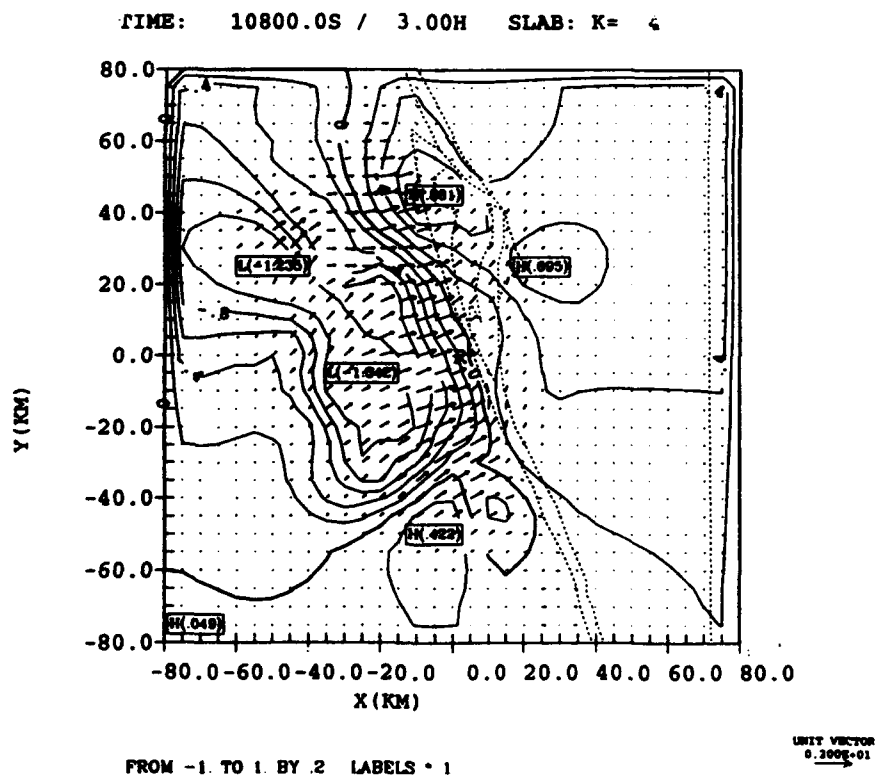
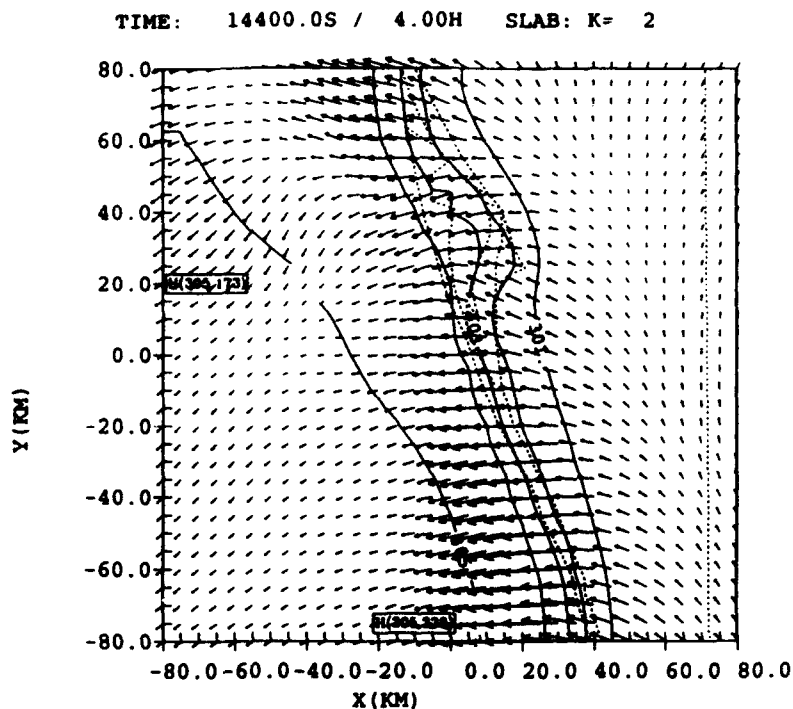


Figure 16: Horizontal cross section of winds and θ at level 4 for hour 3 (17 UTC) of the full assimilation: analysis increments. Dotted line denotes the coastline. The vector scale is given in m/s. The CP4 radar location is shown as the symbol "R".

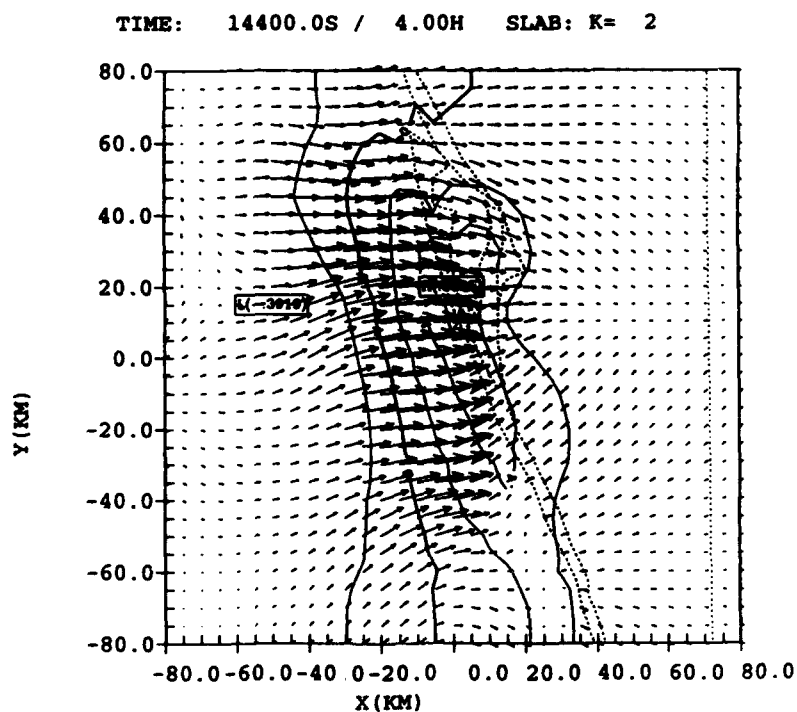
a



FROM 290. TO 330. BY 1. LABELS * 1

UNIT VECTOR
0.500E+01

b



FROM -1. TO 1. BY .2 LABELS * 1

UNIT VECTOR
0.200E+01

Figure 17: Horizontal cross section of winds and θ at level 2 for hour 4 (18 UTC): full assimilation; and differences from control. Dotted line denotes the coastline. The vector scale is given in m/s.

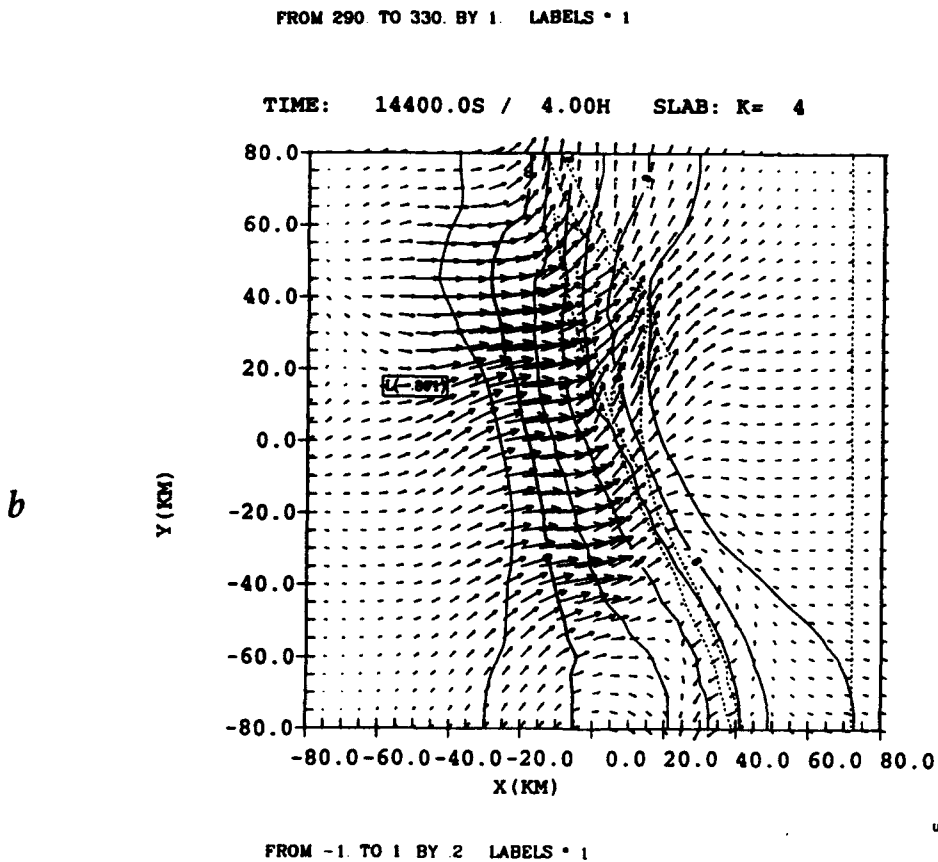
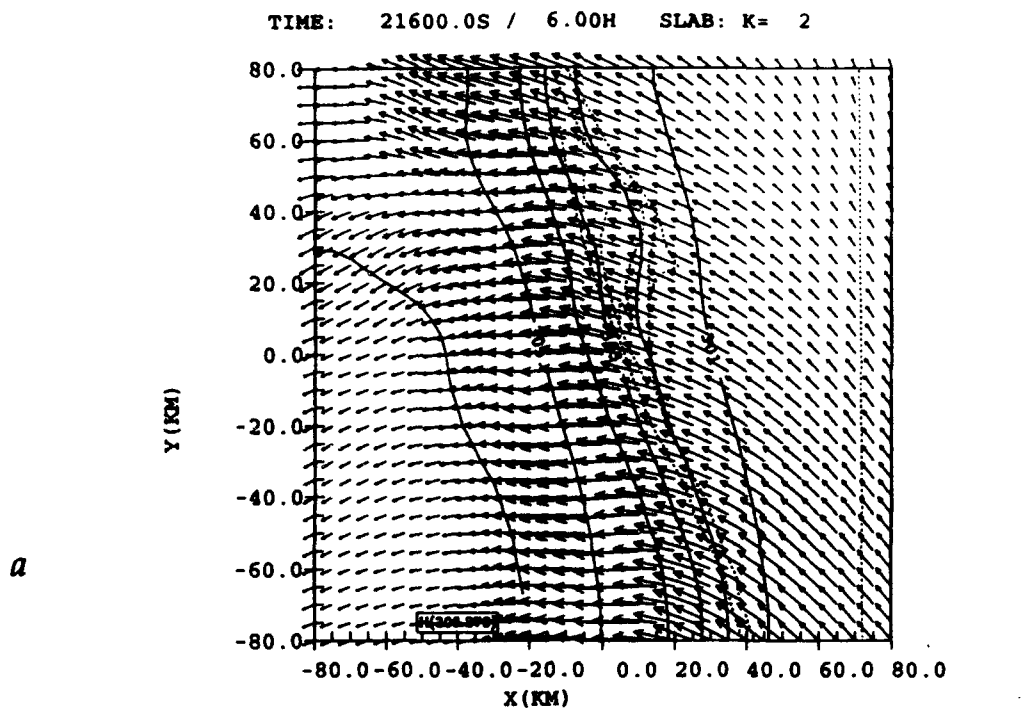


Figure 18: Horizontal cross section of winds and θ at level 4 for hour 4 (18 UTC): full assimilation; and differences from control. Dotted line denotes the coastline. The vector scale is given in m/s.

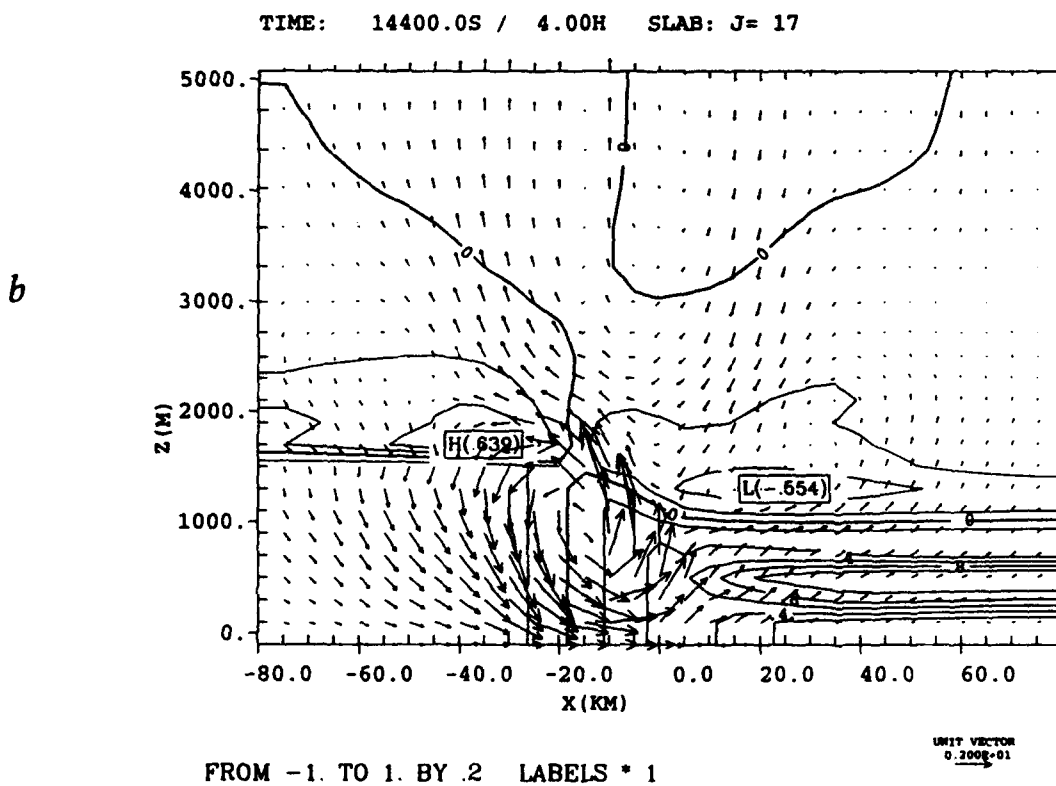
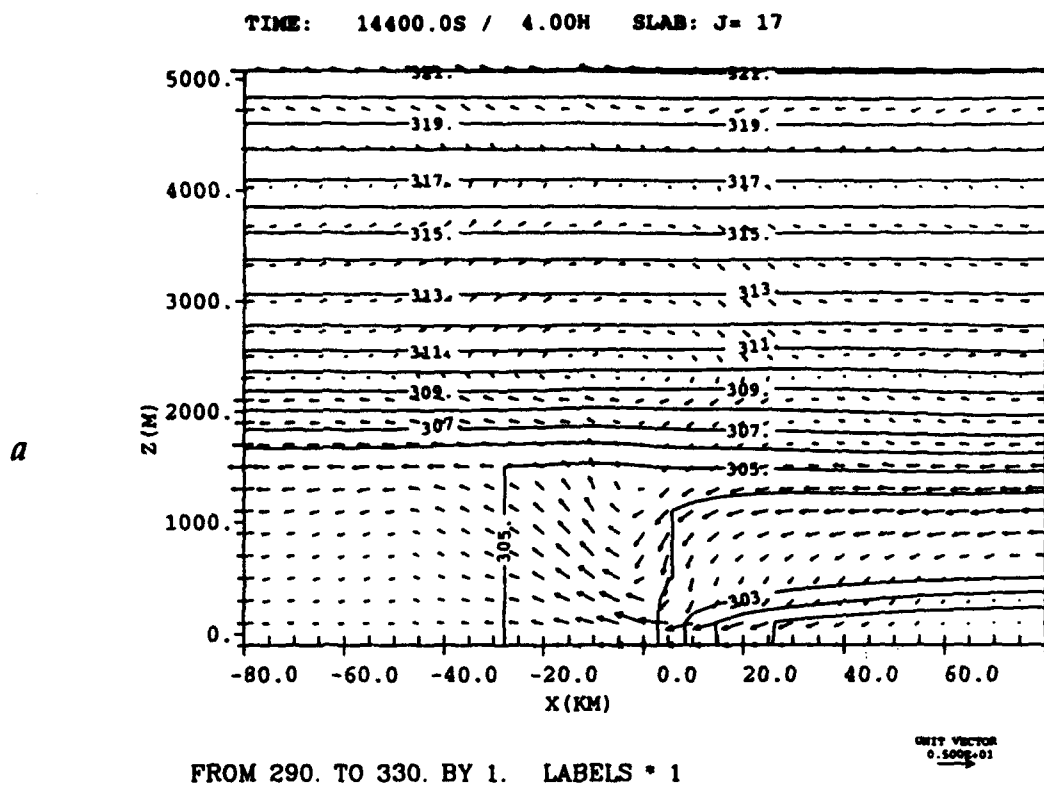
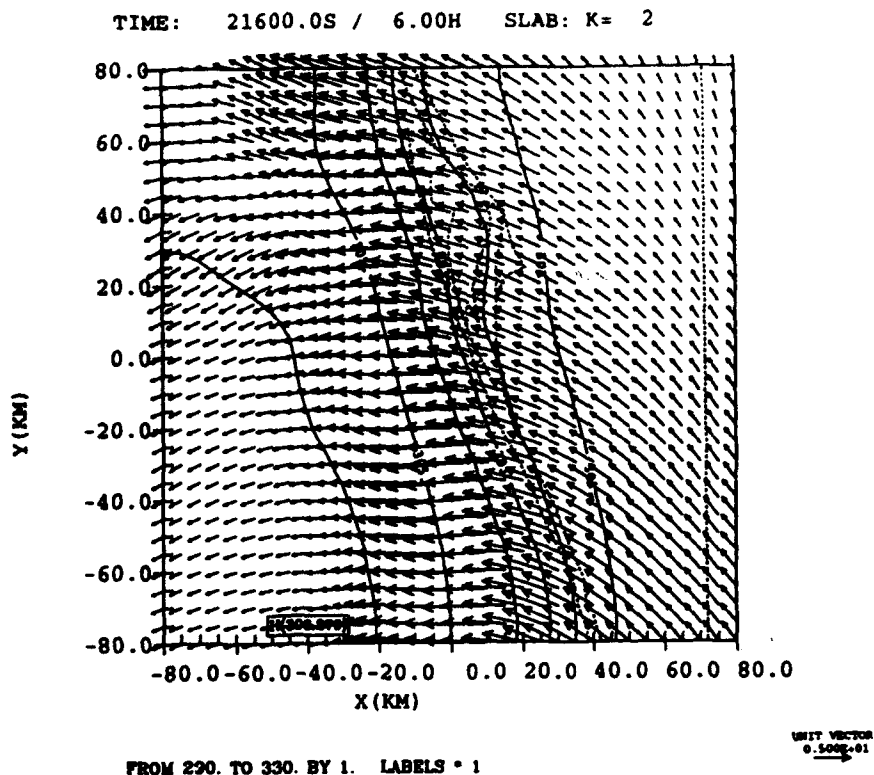


Figure 19: Vertical cross section of winds and θ at $y=0$ for hour 4 (18 UTC): full assimilation; and differences from control.

a



b

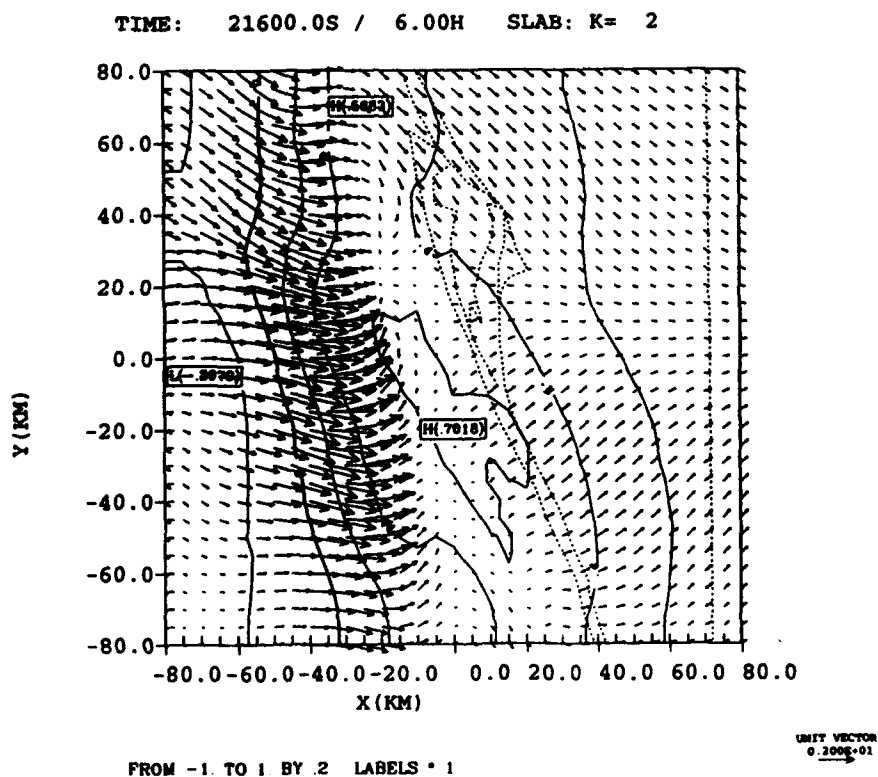
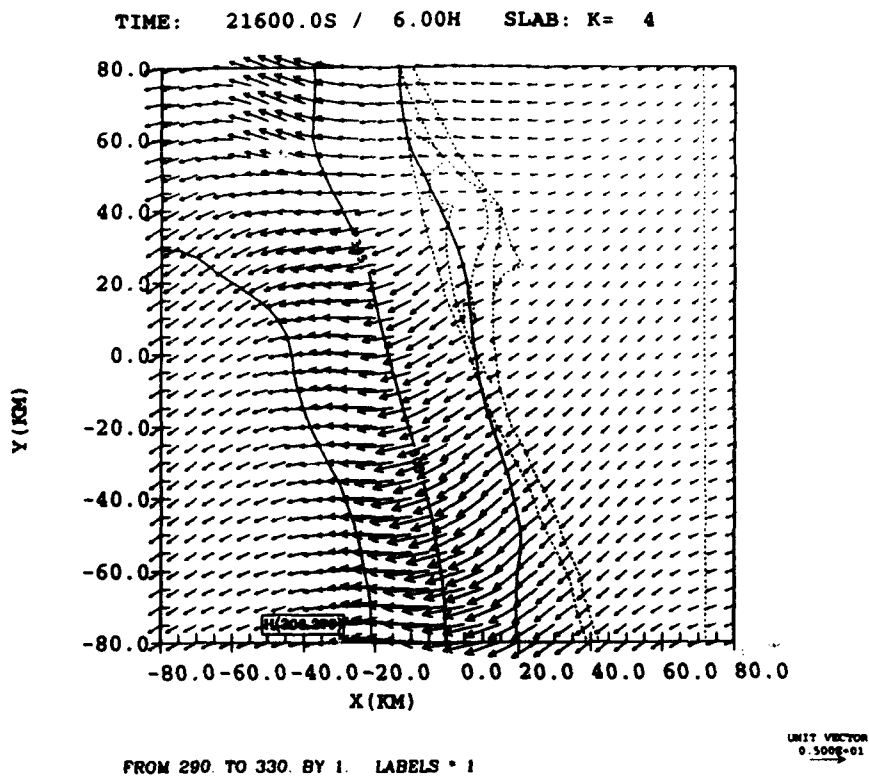


Figure 20: Horizontal cross section of winds and θ at level 2 for hour 6 (20 UTC): full assimilation; and differences from control. Dotted line denotes the coastline. The vector scale is given in m/s.

a



b

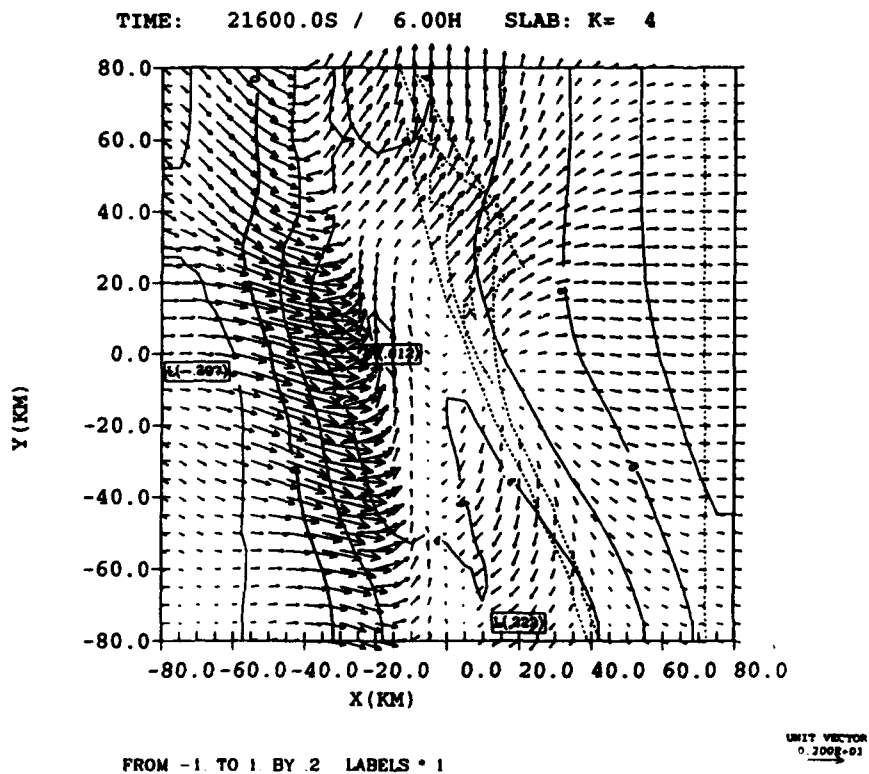


Figure 21: Horizontal cross section of winds and θ at level 4 for hour 6 (20 UTC): full assimilation; and differences from control. Dotted line denotes the coastline. The vector scale is given in m/s.

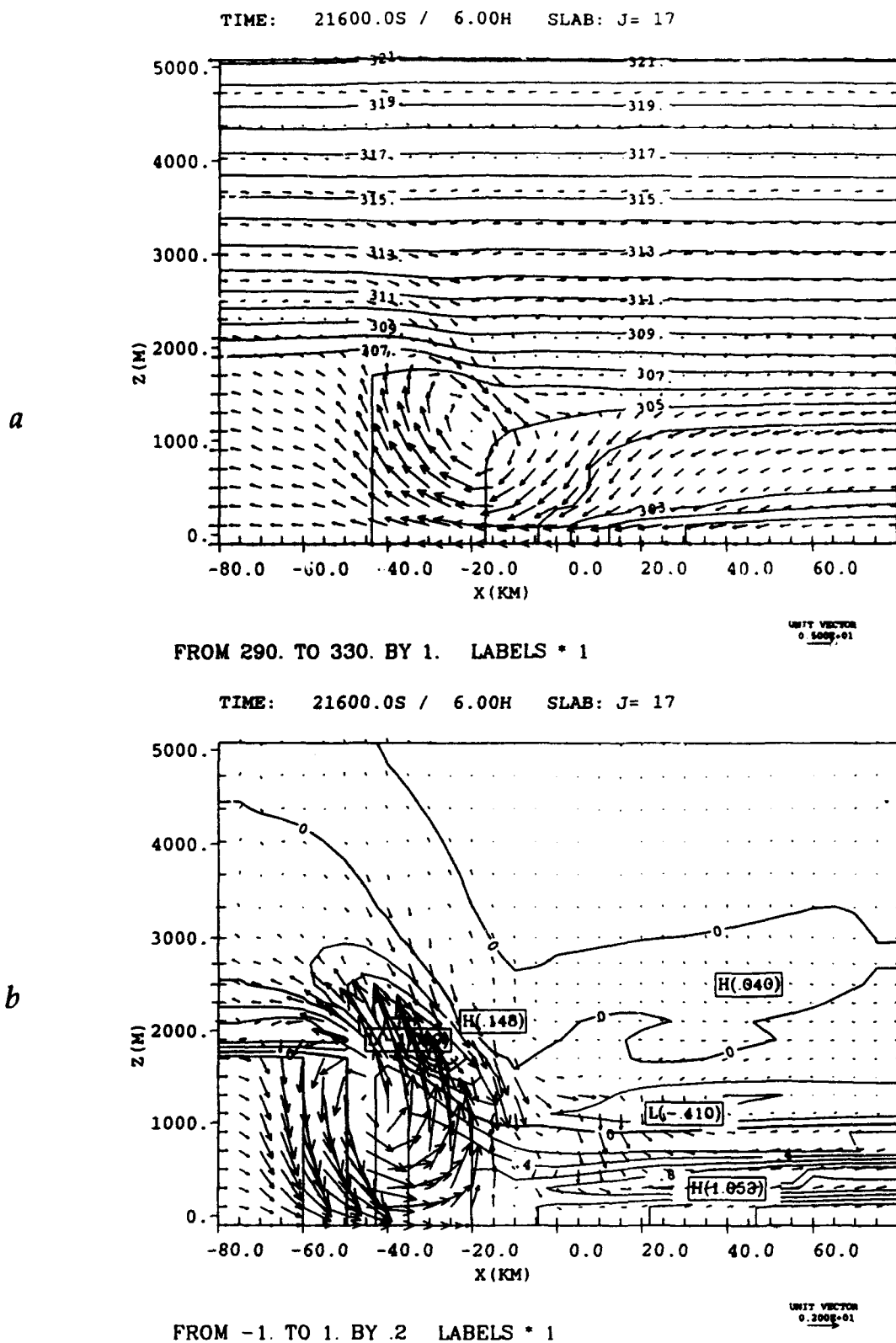


Figure 22: Vertical cross section of winds and θ at $y=0$ for hour 6 (20 UTC): full assimilation; and differences from control.

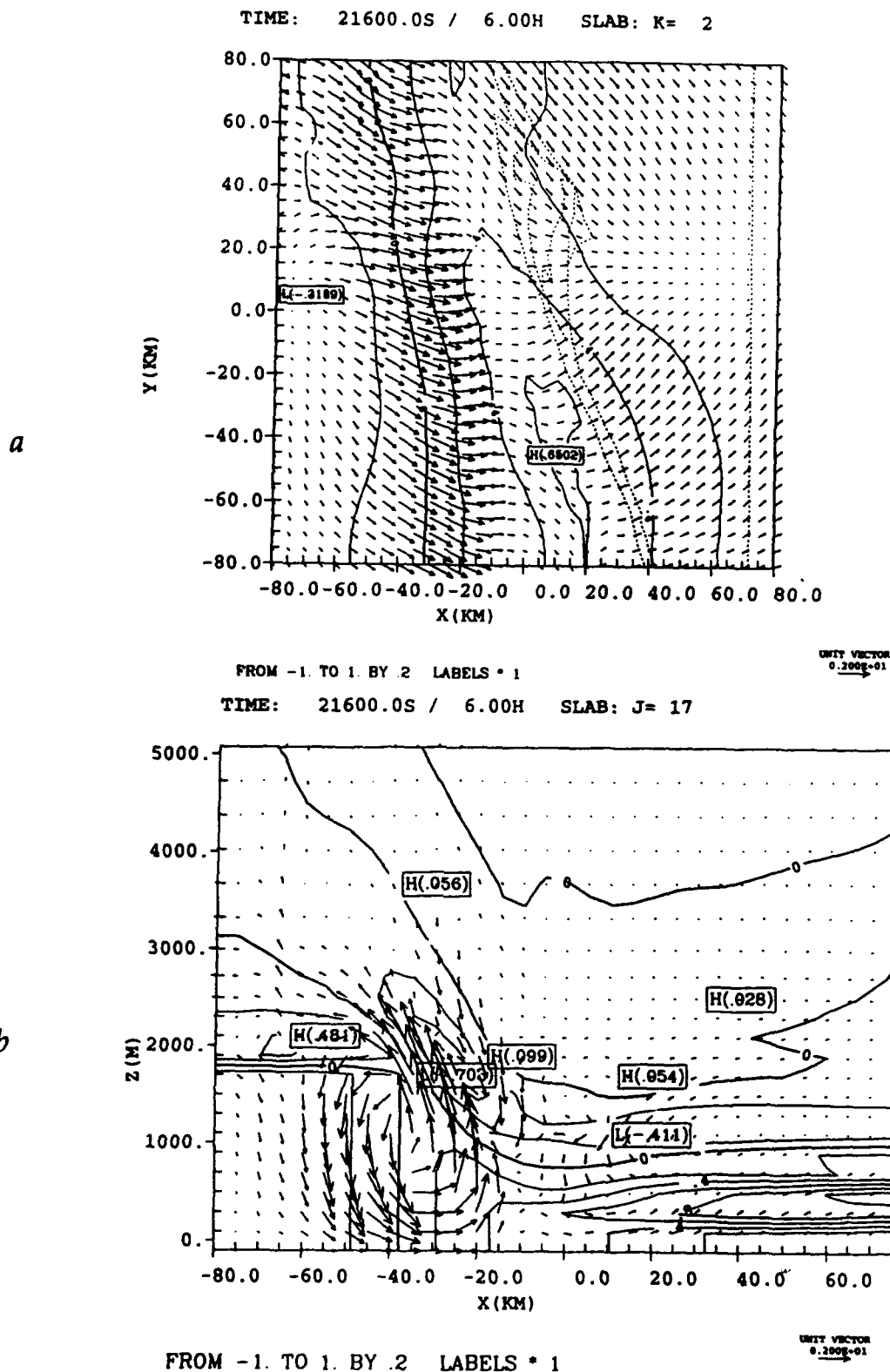


Figure 23: Horizontal cross section at level 2, and vertical cross section at $y=0$, of winds and θ for hour 6 (20 UTC): differences between full assimilation and wind-only assimilation. Dotted line in horizontal cross section denotes the coastline. The vector scale is given in m/s.